2000-C-CT-01-C-42

GOVP1200201054

Creative Research Initiatives

비선형-비평형 다체계의 원리에 기반한 생물학적 단순-신경망의 이해

Nonlinear-nonequilibrium many-body system approach to biological neural network

Center for Neurodynamics

Korea University

Ministry of Science & Technology

제 출 문

과학기술부 장관 귀하

본 보고서를 창의적연구진흥사업의 일환으로 1998년 10월 1일부터 2001년 9월 30일까지 "신경망동력학연구단"에서 연구수행한 "비선형-비평형 다체계의 원리에 기반한 생물학적 단순-신경망의 이해에 관한 연구" 과제의 단계보고서로 제출합니다.

2001 . 11 . 30 .

유치기관명 : 고려대학교
연구단장 : 이경진
연구원 : 이지수
연구원 : 최원규
연구원 : 황종문
연구원 : 김종남
연구원 : 정재승
연구원 : 신종철

SUMMARY

Title: Nonlinear-nonequilibrium many-body system approach to biological neural network

Background:

Biological neural networks that are composed of many interacting nonlinear dynamical units (i.e., neurons) are one of the most important examples of complex systems. They perform computations that have proven very difficult to emulate in conventional digital computers. Researchers have been confronted with three major theoretical issues in trying to understand how real nervous systems achieve their remarkable computational abilities. (a) How can we characterize and understand spatiotemporal activities of neural networks? (b) How do distributed time-varying activities of populations of neurons represent things? (c) How are synaptic strengths adjusted to learn these representations? To really gain insight into these fundamental issues, it is essential (1) to achieve significant understanding on generic self-organizing behaviors of 'complex systems' in general, (2) to develop and study grossly idealized biological neural networks whose features are well defined for quantitative analyses and modeling, (3) to decipher the neural code hidden in the spiking activities of the simplified network. These are our three primary research goals.

Objectives and scope:

The long-term goal of this research project is to build a bridge between nonlinear dynamics and neuroscience, setting a foundation for the new interdisciplinary field *neurodynamics*. The primary research objectives are, (1) to investigate diverse, yet, generic features of spatiotemporal patterns or self-organizations in coupled systems of nonlinear oscillators; (2) to develop simple and well-defined *in vitro* neuronal systems for the quantification of spatiotemporal activities of living biological neural networks; and (3) to understand spiking activities of the simplified network based on nonlinear time series analyses and the theory of pattern formation. During the first three years (1st phase of maximum nine year project), our research emphasis is put on the first objective.

Results:

We revealed several new important phenomena of nonequilibrium pattern formation and successfully developed a proto-type living neural network as a well-defined model system for quantitative study. The most significant results are (1) the first experimental realization of complex periodic spiral waves and associated *line-defects*; (2) the first experimental demonstration of *spatial period-doublings* of basic lattice patterns by resonant mode interactions; (3) the experimental proof that *Substance P* plays a major role in photic resetting of suprachiasmatic nuclus (SCN); and (4) the successful development of a proto-type *neurochip* interfacing biological neural networks with micro-fabricated multi-electrode array (MEA) plate and designed networks of biological cells.

Significance:

During the past three years, we have carried out world-class scientific researches and published several papers in premier research journals **(four in *Phys. Rev. Lett.* and one in *J. of Neuroscience*)** among others. In addition, three papers are currently being reviewed by *Phys. Rev. Lett.* Considering the fact that the total number of papers published in *Phys. Rev. Lett.* by Korean institutions and research centers all together is about 20-30 annually, our scientific achievement as a small research group is quite substantial. Indeed, we are one of the leading groups in the related field, being highly competitive in the international community.

요 약 문

제목: 비선형-비평형 다체계의 원리에 기반한 생물학적 단순-신경망의 이해

연구배경 (연구의 목적 및 필요성):

여러 신경세포들의 결합으로 이루어진 생물학적 신경망은 물리학적인 관점에서 보아 '복잡계'의 패러다임에 속하는 대표적인 생물계이다. 고등동물의 뇌를 구성하는 신경망은 현재의 컴퓨터 알고리즘 및 아키텍쳐로는 모사하기 어려운 고도의 전산학적 기능을 갖는다. 신경망, 더 나아가, 신경계가 수행하는 이 놀라운 기능들에 대한 연구는 크게 세 가지의 근본적인 질문으로 귀결된다. (1) 신경망이 나타내는 전기화학적 신경신호의 시/공간적 특성을 어떠한 방법으로 정량화하고 분석할 것인가? (2) 정량적인 분석과 수학적인 모델링이 가능한 연구대상, 즉, 단순화된 생물학적 신경망을 어떠한 방법으로 이룰 것인가? (3) 신경망이 나타내는 신경신호의 의미는 무엇이며, 이들의 전산학적 기능과는 어떻게 연결되는가?

연구목표 및 범위:

본 연구과제의 목적은 비선형동력학과 기존의 신경생리학의 접목을 통하여, 뉴로다이나믹스라는 새로운 연구 패러다임을 창출하고, 이를 기반으로 생물학적 신경망이 갖는 다양한 생리학 및 전산학적 기능에 대한 이해에 획기적인 발전을 도모하는데 있다. 우선적인 연구목표는, (1) 비선형성을 갖는 진자들의 결합된 연결망에서 보편적으로 나타나는 다양한 자기조직화 현상 및 패턴형성에 대한 연구들을 통하여 비선형-비평형 다체계에서 나타나는 일반적인 현상들에 대한 보편적인 이해를 도모한다, (2) 생물학적 신경세포들의 배양을 통하여 정량적인 분석이 용이한 단순신경망을 미세식각 및 미세도장-전사 기술을 이용하여 능동적으로 이룬다, 그리고 (3) 단순신경망에서 나타나는 신경신호 시계열을 비선형동력학과 비평형문양형성의 다양한 이론적 도구를 적용하여 분석한다. 본 과제의 제 1 단계 3 년 연구는 연구목표 (1)에 보다 큰 비중을 두었다. 제 2 단계 3 년 동안에는 연구목표 (2)와 (3)에 보다 큰 비중을 둘 것이다.

연구내용 및 결과:

제 1 단계 연구기간 동안, 본 연구단은 비평형 문양형성과 관련 몇 가지의 새로운 현상을 발견하여 과학계의 큰 반향을 얻었으며, 또한 실험적 뉴로칩을 개발하여 신경망동력학 실험연구의 초석을 깔았다. 가장 중요한 업적이라 판단되는 몇 가지를 정리하면 다음과 같다: (1) 복잡-주기성을 갖는 나선파와 이와

관계된 결합선의 실험적 구현; (2) 공명모드-상호작용에 의한 단순격자의 주기배가 현상 발견; (3) Suprachiasmatic nuclus (SCN)의 광-위상전이 과정에서 *Substance P*의 역할 규명; (4) 생물학적 신경망과 다중미세전극판(multi-electrode array plate)의 결합을 통한 뉴로-칩의 개발.

기대효과:

지난 1단계 3년의 기간동안 본 연구단에 의하여 수행된 연구 결과들은 국제 과학계의 상당한 반향을 얻었으며, 발표된 연구논문은 관련분야 최고의 국제 학회지에 게제되었다. 현재까지 ***Phys. Rev. Lett.***에 4편, ***J. of Neuroscience***에 1편이 발표되었으며, 또한 3편의 논문이 *Phys. Rev. Lett.*에 제출되어 현재 심사를 받고있다. 대한민국 전체 과학자들이 *Phys. Rev. Lett.*에 발표하는 전체 논문 수가 1년 기준으로 20-30 정도가 됨을 감안할 때, 소규모의 본 연구단이 발표한 논문 4편은 상당한 업적이라 판단된다.

Table of Contents

Chapter 1 : Introduction

Chapter 2 : State of the art

Chapter 3 : Method, Results and Discussion

Chapter 4 : Conclusion

Chapter 5 : Major Contribution

References

Appendix

Chapter 1. Introduction

Steven Hawking recently asserted that **complex systems** would be the most important science of the 21st century. Very influential Nobel laureates, M. Gellman and P. Anderson recently wrote several articles addressing the importance of the new interdisciplinary science as well. Indeed, complex systems are very challenging up-to-date scientific issues [see for example, Science Vol. 284 (1999)], and from our viewpoint **'nonequilibrium pattern formation'**[1], is believed to be the most systematic approach towards the understanding of seemingly universal self-organizing behaviors of complex systems.

Biological neural networks that are composed of many interacting nonlinear dynamical units (i.e., neurons) are one of the most important examples of complex systems. They perform computations that have proven very difficult to emulate in conventional digital computers. Researchers have been confronted with three major theoretical issues in trying to understand how real nervous systems achieve their remarkable computational abilities. (a) How can we characterize and understand spatiotemporal activities of neural networks? (b) How do distributed time-varying activities of populations of neurons represent things? (c) How are synaptic strengths adjusted to learn these representations? To really gain insight into these fundamental issues, it is essential (1) to achieve significant understanding on generic self-organizing behaviors of **'complex systems'** in general, (2) to develop and study grossly **idealized biological neural networks** whose features are well defined for quantitative analyses and modeling, (3) to decipher the neural code hidden in the spiking activities of the simplified network. These are our three primary research goals.

We have seen a recent dramatic increase in our knowledge of the genes and molecules that control key biological events, but similar advances have not yet come about in our understanding of the principles that govern the massively complex neuronal system or *brain*. Clearly, some kind of theory is needed if it is ever to be understood. It can be achieved only by understanding the rich interplay of highly nonlinear intrinsic properties of individual neurons and the coupling properties between cells that determine the spatiotemporal activity of the neuronal network. Our research team is at the forefront of this line of investigation with strong background in nonlinear dynamics.

---

[1] M. Cross and P.C. Hohenberg, Rev. Mod. Phys. 65, 851 (1993).

Chapter 2. State of the art

Section 2.A. Research trends in the relevant international community

Section 2.A.1) Nonequilibrium pattern formation

The international community studying nonequilibrium pattern formation has grown steadily over the last decade, and the topic *nonequilibrium pattern formation* has become broader in conjunction with the rapidly growing interest in complex system studies in general. There are now several annual conferences on closely related issues including two Gordon Research Conferences. New topics emerge every year and the focus of concentration shifts. Some latest research topics that are relevant to our project are: spatiotemporal dynamics of defects (point singularity, line-defects, string, etc); pattern formation by multi-mode nonlinear resonant interactions; and dynamics of nonlinear systems under background noise, internal feedback, or external forcing. Our current researches lie at the forefront of these up-to-date issues leading the community worldwide. Some of leading groups who are relevant to us are Kapral group at Univ. of Toronto, Bodenschatz group at Cornell University, Ertl groups at Max Plank Institute, and Swinney group at Univ. of Texas at Austin.

The Kapral group leads the community studying chemical instabilities in theory and computation. Their recent study on complex periodic spiral waves, in particular, has brought a great excitement to the community[2] [3] [4] Indeed, our experiments on chemical wave patterns are in part motivated by their theoretical and numerical findings. More recently, they have conducted a series of massive computation of three dimensional scroll wave and investigated the associated dynamics of filament (the topological defect of a 3D scroll) [private communication]. We are currently collaborating with them very closely.

The Swinney group at Univ. of Texas and the Ertl group at MPI both run a major research center investigating chemical patterns among other things. Both groups are now investigating effects of forcing given to pattern forming system. More specifically, the Swinney group has investigated effects

---

[2] L. Goryachev and R. Kapral, Phys. Rev. Lett. **76**, 1619 (1996).
[3] L. Goryachev, H. Chaté, R. Kapral, Phys. Rev. Lett. **80**, 873 (1998).
[4] L. Goryachev, H. Chaté, R. Kapral, Phys. Rev. Lett. **83**, 1878 (1999).

of homogeneous extrinsic forcing given to an oscillatory chemical medium near a Hopf bifurcation. They have found various resonant patterns, generating interesting theoretical issues. More recently, Ertl group has studied a similar system but with an internal feedback loop as versus to the external forcing used by the Texas group. They also found a variety of new patterns not been characterized before.

The Cornell group led by E. Bodenschatz is studying nonequilibrium patterns in fluid systems, mainly Rayleigh-Benard convection systems. They are famous for reporting Spiral Defect Chaos (SDC) in a Rayleigh-Benard. One of their current research interests is to understand the bistability between Ideal Straight Rolls (ISR) and SDC. Related topic is the dynamics of interface separating domains of two different dynamical states.

Section 2.A.2) Neurodynamics

The current community of neurodyanmics is basically a group of scientists, about one half of which has an expertise on nonlinear dynamics and the other half has background in computational neuroscience. At any case, they are theoreticians mostly.

One important issue recently brought by this community is Stochastic Resonance (SR). SR means that there is an optimal strength of environmental noise that maximizes the signal to noise ratio or the performance of the concerned system (often, an input/output device). The group of Frank Moss at Univ. of Missouri has pioneered this field few years ago. Since then, SR has been demonstrated in numerous systems including several different neuronal systems. From our viewpoint, however, SR is just a simple generic phenomenon of noisy nonlinear system. Analyzing (or separating out) effects of external noise in neuronal signal seem to be a much more fundamental issue. There are now several theory groups investigating such issues, using various model systems. Longtin at Univ. of Ottawa, J. Collins at Boston Univ., and K. Pakdaman at CNRS are the most active researchers among others in the field.

There are many different views of what models of neuronal systems should achieve, and the diversity is reflected in the variety of research topics of modern computational neurosciences. Some of the most notable ones are the followings. Koch (Caltech) and Segev (Hebrew University), for example, strongly believe in information processing in single neurons. Their modeling involves quite the details of a single neuron, including synapses, ion channels and even the detailed morphology of dendrites. Recently, they have succeeded to show that such a faithful neuron model can be a sophisticated processor with mixed analog-digital logic. The key challenge for the success of this approach, however, is have the detailed knowledge of the relevant biophysical mechanisms that are not much accomplished at this time. At the other end of the spectrum, Dayan (University College London) discusses statistical models of learning, relating these to the phenomenon of attention at a level of abstraction that is still some distance from the underlying neural processes. Taking a very different approach, Mauk (Univ. of Texas Medical School) attempt to build a simulation of the cerebellum based on its known circuitry. In a sense, the field is so young that a general consensus has not yet emerged.

Section 2.B Research trends in the relevant domestic community

With the influx of foreign educated young Korean researchers in the related field and the growth of existing community within the country, there is now a sizable nonlinear dynamics society with about 200 participants in Korea. The participants conduct researches on various aspects of nonlinear dynamics and nonequilibrium patterns employing different systems, ranging from driven granular materials (H. Moon at KAIST, Pak at Pusan Nat'l Univ.), Josephson junction array (D. Kim and M. Choi at SNU, S. Kim at POSTECH), Driven nonlinear oscillators (Y. Kim at Ajou Univ. and S. Kim at Kwangwon Nat'l Univ.), nonlinear optical systems (T. Kim at Korea Univ. and C. Kim at Baeje Univ.), etc.

With the rapid expansion of brain sciences and the emergence of complex system paradigm, the new interdisciplinary field neurodynamics is formed over the last several years, and some core participants of the nonlinear dynamics community (for example, S. Kim at POSTECH, S. Han at Chungbuk Nat'l Univ., T. Kuck at Kyungwon Univ.) now study issues in computational neuroscience in relation to nonlinear dynamics and nonlinear time series analysis. Their approach is, however, limited to model studies based on numerical computations.

Section 2.C Things that distinguish us from others in the field

There are hundreds of thousands researchers conducting various aspects of *brain* or biological neural networks all over the world. Similarly, there are thousands of physicists, mathematicians, and engineers who are investigating different aspects of nonlinear systems. Neurodynamics has emerged only recently to fill the gap between nonlinear dynamics of complex systems and brain science, and the community of neurodynamics is in its infancy. Our center is at the forefront leading the community internationally as well as within the nation. In fact, our center is the first place studying nonlinear dynamical aspects (i.e. from the context of nonequilibrium patterns) of biological neural networks in well-defined experimental systems, along with theoretical analysis and modeling based on nonlinear dynamics.

Now the community seems to well appreciate the importance of our scientific approach that is based on actively formed simple *in vitro* neural networks. Here, we note that a new research center that is quite similar to ours is just formed at Caltech led by Steve M. Potter with a strong support from National Institute of Health (USA). Their philosophy is the same as ours, but their research focus is more on a specific physiological issue such as *learning*. They have very good knowledge and experience in neuroscience in general and well-equipped, but do not have much background in dynamical system theory.

Chapter 3. Method, Results and Discussion

Section 3.A Complex periodic spirals and line-defect mediated spatio-temporal chaos

Recent numerical simulations on two-dimensional model reaction-diffusion systems have revealed unusual spiral waves with complex oscillations and turbulent patterns, both mediated by "line-defects". Here we report the observation of such patterns in a laboratory experiment for the first time; complex spiral waves with period-2 and period-3 and turbulent patterns filled with a tangle of line-defects are observed and their spatio-temporal dynamics are elucidated by line-defects. Since line-defects are a generic property of complex periodic media, the observed patterns are to arise in a broad class of complex periodic systems.

Section 3.A.1) Motivation and Background

"Complex systems" that are composed of many interacting nonlinear dynamical units can self-organize to exhibit various spatio-temporal patterns. Such systems are ubiquitous in nature[5] and various scientific issues regarding them have emerged recently in different disciplines including physics[1,6], chemistry[7,8], biology[9,10,11], and ecology.[12,13] Among others, of particular interest is the spatio-temporal dynamics in a system of coupled chaotic oscillators. Recent computer simulation studies on a such system have revealed unusual spiral waves with multiple periods (period-2"), period-doubling cascade in space, and turbulent patterns.[2,3,4] The most striking feature of these patterns is the existence of "line-defects" across which the phase of local oscillation changes by a multiple of 2π. Here we report the experimental observation of period-2 (P-2) and period-3 (P-3) spirals and line-defect mediated turbulence employing a novel nonlinear chemical reaction-diffusion system.

---

[5] R. Gallagher *et al.*, Science **284**, 79 (1999), Special section on complex systems.
[6] D. Walgraef, *Spatio-Temporal Pattern Formation* (Springer, New York, 1997).
[7] *Waves and Patterns in Chemical and Biological Media* H. L. Swinney and V. I. Krinsky (MIT/North-Holland, 1992).
[8] *Chemical Waves and Patterns*, edited by R. Kapral and K. Showalter (Kluwer, Dordrecht, 1995).
[9] L. Rensing, *Oscillations and Morphogenesis* (Marcel Dekker, New York, 1993).
[10] L. Glass, Physics Today **45**, No 8, 40 (1996).
[11] C. M. Hempel, P. Vincent, S. R. Adams, R. Y. Tsien, and A. I. Selverston, Nature **384**, 166 (1996).
[12] E. Ranta and V. Kaitala, Nature **390**, 456 (1997).
[13] B. Blasius, A. Huppert and L. Stone, Nature **399**, 354 (1999).

Section 3.A.2) Method

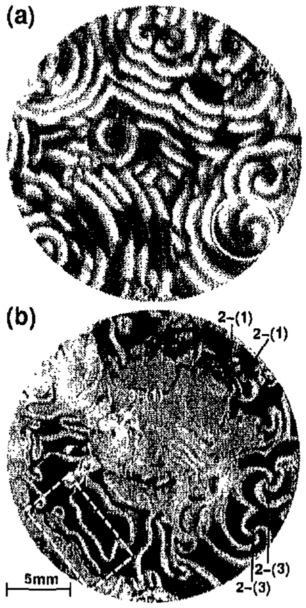

FIG. 3.A.1. Snapshot image of a complex periodic pattern observed in a BZ system (a); and processed image revealing line-defects and domains of P-2 and P-3 in (a) (b). The flow rate is fixed at 120±1ml/h. In the raw images (a), white and black represent the oxidized and reduced states, respectively. The image in (b) shows a scalar field, $\Delta V(t) = \frac{1}{2\pi}\int_0^{3\pi} \left|V(\bar{r},t+t') - V(\bar{r},t+3\tau+t')\right| dt'$, where $V(\bar{r},t)$ is the grey value in the raw images associated with (a). P-2 domain (black) has a higher value of ΔV than the one of P-3 domain (light grrey). Some spiral cores are labeled by "u – (v)", where u = period and v = number of line-defects emanating from the core. The narrow light grey stripes are line-defects.

Our experiments were conducted with Belousov-Zhabotinsky (BZ) reaction whose homogeneous temporal dynamics can be excitable, simple and complex periodic, and chaotic.[14] [15] Until recently studies on patterns using this reaction were mainly focused on simple periodic spiral waves that form when the underlying chemical kinetic is excitable or simply oscillatory.[16] [17] In our experiments, a BZ system whose underlying chemical kinetics is complex periodic or chaotic is emploied.

The patterns form in a thin transparent polyacrylamide gel membrane 0.65mm thick, 25mm diameter) sandwiched between two reservoirs of reagents. The gel medium, which is inert to the chemical reaction, guarantees the necessary reaction-diffusion nature. The two well-stirred reservoirs are continuously refreshed with the reagents of the reaction. The reaction occurs in the gel medium where the two groups of reagents meet. For the parameter regime that we explored, there is no dynamics in the reservoirs. The flow rate of the reagents is used as a control parameter with other parameters fixed.

We first discuss the pattern observed in a high flow rate regime. Within several hours beginning the experiment, the reacting medium establishes a steady state that is visually very complex [Fig. 3.A.1(a)]. A careful investigation on this dynamic state, however, reveals that the whole pattern is

---

[14] R. H. Simoyi, A. Wolf, H. L. Swinney, Phys. Rev. Lett. **49**, 245 (1982).
[15] K. S. Scott, *Chemical Chaos* (Clarendon Press, Oxford, 1991).
[16] A. T. Winfree and S. H. Strogatz, Nature **311**, 611 (1984).
[17] A. S. Mikhailov, *Foundation of Synergetics I. Distributed Active Systems* (Springer-Verlag, Berlin, 1994).

organized by spiral cores that either have P-2, P-3, or mixed (P-2/P-3) periods, and line-defects [Fig.3.A.1(b)]. We first focus on the structures and the dynamics of the spiral cores.

Section 3.A.3) Results

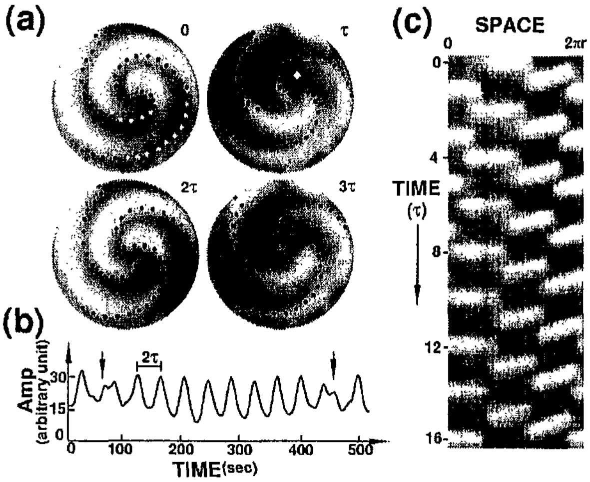

FIG. 3.A.2. Structure and temporal evolution of a P-2 spiral: (a) snapshots of a P-2 spiral with three spiraling line-defects (black dotted line) taken at every $\tau = 24$ sec; (b) local time series taken at the location of diamond in (a); and (c) space-time plot taken along a circle centered at the spiral core with a radius r = 1.3mm. The line-defects are obtained according to the process explained in the legend of Fig. 3.A.1. The white dotted line in t = 0 of (a) is drawn following an assumed profile of P-1 spiral for visual guide. The angular velocity of the three line-defects is about 0.42 rad/min.

Figure 3.A.2(a) shows an evolution of a P-2 spiral core [encircled area in Fig. 3.A.1(a)]. The image clearly repeats at every 2τ, where τ is the period of a fundamental (P-1) oscillation. The rotational symmetry of a P-1 spiral (guided by white dotted line) is broken by the presence of three line-defects (black dotted lines) spiraling out from the core. That is, the phase of local oscillation along the white dotted line changes by 2π (light grey - black transition) crossing a line-defect. The topological continuity of a P-2 spiral requires an odd number of line-defects originating from the core[3] and the P-2 spiral shown in Fig. 3.A.2(a), in particular, has three line-defects. Shown in Fig. 3.A.2(b) is a typical local time series obtained at a fixed location. The time series is basically P-2 except for some occasional disturbances (indicated by black arrows). The presence of these disturbances is due to the movement of line-defects. Figure 3.A.2(c) clearly illustrates that three line-defects rotate more or less steadily in counter-clockwise direction. The local dynamics within a line-defect is basically P-1; hence, a short disturbance of P-1 appears in the local time series whenever a line-defect sweeps passing the measuring site.

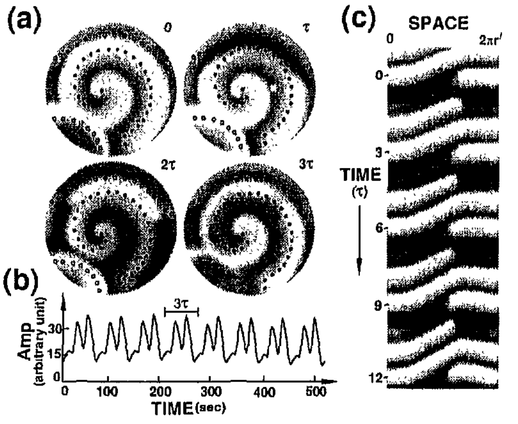

FIG. 3.A.3. Structure and temporal evolution of a P-3 spiral: (a) snapshots of a P-3 spiral with a line-defect (black dotted line); (b) local time series taken at the location of square in (a); and (c) space-time plot taken along a circle centered at the spiral core with a radius $r' = 1.2$mm. The two open dotted lines in (a) are also line-defects but originating from other neighboring sources.

Period-3 (P-3) spirals are also observed under the same condition with which P-2 spirals are obtained [Fig. 3.A.3(a)]. Like P-2 spirals, P-3 spirals also need line-defects to exist. Any number of line-defects except the multi ples of three would be allowed for a P-3 spiral; the example shown in Fig. 3.A.3(a), in particular, has a single line-defect. The spiraling nature of the line-defect is very similar to the ones in Fig. 3.A.2(a), but here the shape of the line-defect is almost the same as the profile of the P-3 spiral itself - therefore, the whole spiral undergoes a 2π phase shift simultaneously as it rotates passing the line-defect. Unlike the line-defects of P-2 spiral shown in Fig. 3.A.2, the line-defect in this example barely moves: the local time series [Fig. 3.A.3(b)] shows no disturbance for the period of observation and the space-time plot [Fig. 3.A.3(c)] shows no significant motion of phase line-defect.

These spiral cores govern the temporal and morphological structure of the whole system as in a conventional excitable system. Here, they are the sources forming domains of P-2 and P-3 [Fig. 3.A.1(b)]. The large central region and the narrow region along the left half boundary (light grey area) are revealed to be P-3, whereas the remaining domain (black area) is P-2. Line-defects appear as narrow strips. A pair of three spiraling line-defects associated with a pair of P-2 spirals is clear in the lower right-hand side of Fig. 3.A.1(b). Some P-2 spirals with a single line-defect and a small P-3 spiral are also observed in the same medium as marked. The structure of line-defects around the marked P-3 spiral near the central region is not clearly resolved in Fig. 3.A.1(b), but in a different method we have identified a single line-defect spiraling out from the core as in Fig. 3.A.3(a) but winding very tightly in a quite irregular manner. In general, the number and the shape of line-defects originating from a spiral core depend strongly on the neighboring environment.

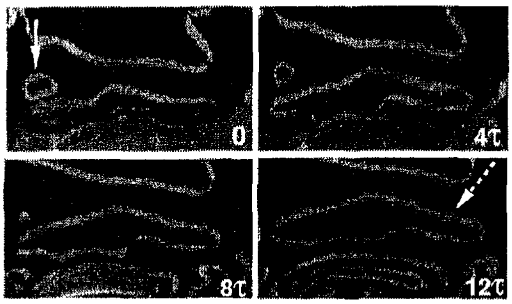

FIG. 3..A.4. The birth and death of bubble-shaped line-defects. The sequence of images [8.0 × 4.8mm^2 boxed area in Fig. 3.A.1(b)] showing a decay of spontaneously formed bubble (indicated by a solid white arrow) and a proliferation of large flat bubble (indicated by a dashed white arrow) from a boundary separating P-2/P-3 domains.

Line-defects can also exist in various forms of simply connected loops ("bubbles"), not being associated with a spiral core. There are two different kinds. First, bubbles can nucleate spontaneously in an area devoid of line-defects. They usually grow to a critical size (but to an arbitrary shape) and decay gradually (see Fig. 3.A.4). Second, some bubbles can proliferate from the boundary separating domains of different periods: see the bottom halves of the sequential images in Fig. 3.A.4, where the black P-3 domain "opens up" to produce a stack of line-defects. This stack in turn produces a series of big and flat bubbles which drift away. The moving direction and the speed of bubbles fluctuate significantly from one to other places. Line-defects also connect each other upon collision in a seemingly random fashion.

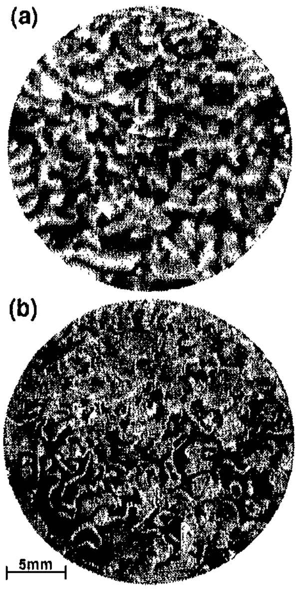

FIG. 3.A.5. Snapshot image of a turbulent state mediated by line-defects in a BZ system (a); and processed image revealing line-defects and fragmented small domains of P-3 (light grey domains) (b). The grey scales used for (a) and (b) and the image processing scheme for (b) are the same as in Fig. 3.A.1. The flow rate is 100 ± 1 ml/hr.

At lower flow rate of the chemical reagents, the reacting medium becomes quite turbulent. Small wave segments with irregular shapes constantly appear and decay without any discernible periodicity [Fig. 3.A.5(a)]. The complexities of the pattern again can be better understood with a processed image [Fig. 3.A.5(b)]. The features of Fig. 3.A.5(b) are very different from the ones of Fig. 3.A.1(b) in several significant ways. First, the line-defects in Fig. 3.A.5(b) are much thinner than the ones in Fig. 3.A.1(b) -- a good indication that the 2π phase change occurs faster here. Second, the domains of different periods are still visible but fragmented into much smaller pieces. Third, the density of line-defect is much higher; in particular, the number of small bubbles has increased significantly.

With the fast and complex evolution of line-defects and small domains, the long-time local time series at a fixed location can not be distinguished from the low-dimensional chaos seen in homogeneous BZ reaction[1, 4]. These observations convincingly suggest that the turbulent state shown in Fig. 3.A.5(a) is indeed mediated by line-defects as in[4].

Section 3.A.4) Discussion

Our results raise a number of interesting questions. Dynamical systems exhibiting a period doubling cascade, such as the BZ reaction, would likely to show P-2^n (n: non-negative integer) spirals.[2, 3] So far, our experiments have revealed only P-2 and P-3 spirals, and no P-2^n ($n \geq 2$) spirals. The reason for this is not obvious. The stabilities of spirals with different periods and shapes in relation to line-defects need to be studied. Also, the observed dynamics of bubbles and the mechanisms for the creation (and decay) of them are yet to be elucidated. The transition to line-defect mediated turbulence also needs to be quantified. Further experiments on the same system may help shed light on these questions.

Section 3.B Formation of spiraling line-defects and its meandering transition in a period-2 oscillatory medium

The instability of a period-1 spiral wave resulting a period-2 spiral wave with a line-defect is investigated for the first time in a laboratory system. At the very onset the transition proceeds by an emergence of spiraling line-defect, “breathing" intermittently but retaining the symmetry of a period-1 spiral wave. With a further change in a control parameter, the line-defect undergoes a meandering transition producing a compound tip trajectory, following a dynamic shape transition. The observed phenomena have strong analogy to the phase synchronization transition of a system of two coupled nonlinear oscillators and the meandering transition of a period-1 spiral wave.

Section 3.B.1) Motivation and Background

Spiral wave is perhaps the best characterized dissipative structure known to exist in spatially extended nonequilibrium media. Studies on this structure are abundant in literature in various contexts.[7,8,18,19,20,21,10] A significant amount of work has been already devoted to understand the underlying pattern forming mechanism, shape, dispersion relation, core dynamics[22], and more recently various roles in biological sciences.[10,21,23] However, previous studies had mostly focussed on simple spiral waves that arise in excitable or simply periodic media until a few years ago when Goryachev *et. al.* revealed complex periodic [i.e., other than period-1 (P-1)] spiral waves in numerical simulations on a diffusively coupled network of Rüssler oscillators.[24]

Their result is very significant to show that complex periodic spiral waves are generically associated with "line-defects" on which two selected loops of a period-n cycle exchange. Therefore, in a period-2 (P-2) medium line-defect is a string of spatial points at which local oscillation is temporally P-1. Our earlier experiment subsequently demonstrated the existence of complex period spiral waves and the associated line-defects in a laboratory system.[25] Thus line-defects seem to be a generic property of complex periodic spiral wave, just as the topological (phase) singularity is a fundamental property of simply periodic P-1 spiral wave. Since line-defects underlie the whole morphology and the temporal behavior of the complex periodic waves, it is essential to understand their spatio-temporal dynamics and bifurcations.

Here, our experimental study focuses at the instability of a P-1 spiral wave leading to a P-2 spiral wave and subsequent changes in the spatio-temporal dynamics of the associated line-defect. At the very onset of transition, the temporal P-1 symmetry breaks in an intermittent fashion while the spatial continuity of a P-1 spiral is retained. With a subsequent change in a control parameter, the spatial continuity breaks as the line-defect transforms its shape. Almost immediately following this spatial symmetry breaking, the tip of line-defect exhibits a well defined meandering transition resulting a compound tip trajectory.

---

[18] A. T. Winfree, *When time breaks down* (Princeton University Press, Princeton, 1987).

[19] G. Ertl, Science **254**, 1750 (1991).

[20] K. B. Migler and R. B. Meyer, Phys. Rev. E **48**, 1218 (1993).

[21] K. J. Lee, E. C. Cox, and R. E. Goldstein, Phys. Rev. Lett. **76**, 1174 (1996) and Pálsson, K. J. Lee, R. E. Goldstein, J. Franke, R. H. Kessin, and E. C. Cox, Proc. Natl. Acad. Sci. USA **94**, 13719 (1997) and references therein.

[22] A. S. Mikhailov, *Foundation of Synergetics I. Distributed Active Systems* (Springer-Verlag, Berlin, 1994) and references therein.

[23] J. Lechleiter, S. Girard, D. Clapham, and E. Peralta, Nature **350**, 505 (1991); L. Rensing, *Oscillations and Morphogenesis* (Marcel Dekker, New York, 1993).

[24] A. Goryachev, H. Chaté, R. Kapral, Phys. Rev. Lett. **83**, 1878 (1999) and references therein.

[25] J. -S. Park and K. J. Lee, Phys. Rev. Lett. **83**, 5393 (1999).

Section 3.B.2) Method

These transition are observed in a well-controlled gel reactor employing a BZ chemical reaction. The reactor is composed with a thin composite slab of porous medium [a transparent polyacrylamide gel membrane (0.60 mm thick, 22 mm diameter), supported by a white nitro-cellulose membrane for visual background and by an Anopore disk for structural support] and two reservoirs that are constantly replenished with a mixture of reagents. Each side of porous medium has a direct contact with the stirred pool of chemical reactants in the reservoirs (Side I: 0.87 - 1.51 M and 0.75 M H_2SO_4 and 0.75 M $NaBrO_3$; Side II: 0.53 M $CH_2(COOH)_2$, 2.5 mM *ferroin*, 0.1 mM *NaBr*, and 0.1 mM *SDS*, each volume 10ml). The flowrate is fixed at 120 ml/hr and the reactor temperature is regulated at 22.0 ± 0.2^0. Only the input acid concentration $[H^+]$ is used as a control parameter with other parameters fixed.

Section 3.B.3) Results

Traveling waves form in the gel slab where the two groups of reagents meet. They are usually initiated spontaneously from the gel boundary or from random pacemakers as the chemical reactants are fed into the gel membrane. In a high $[H^+]$ regime, the system is simply periodic (i.e., P-1), producing well known BZ spiral wave that is simply periodic [top frame of Fig. 3.B.1(a)]. A P-1 wave train [first timeseries in Fig. 3.B.2(a)] emanates continuously out from the spiral core as the spiral rotates steadily. The profile of a P-1 spiral wave is continuous and has no defect except for the singular point at the core. The corresponding scalar field (ΔV) image [bottom frame of Fig. 3.B.1(a)] revealing the local periodicity in grey scale naturally shows no structure.

As $[H^+]$ is lowered, the homogeneous kinetics undergoes a period doubling bifurcation. Near this transition, the P-1 spiral wave becomes unstable as well, but first in time domain only. The initially regular local P-1 timeseries becomes irregular with the emergence of intermittent "P-2 episodes" - brief interventions of P-2 signals in an otherwise P-1 signal - as marked by the arrows [second timeseries in Fig. 3.B.2(a)]. During this intermittent local oscillation, however, the continuous morphology of the initial P-1 spiral is still unaltered by the emergence of a "breathing" line-defect which has the same spatial symmetry of a P-1 spiral wave as shown in Fig. 3.B.3. The breathing line-defect appears (or disappears) in an exact accordance with the emergence (or disappearance) of a P-2 episode in the local timeseries. Naturally, the width of the breathing line-defect varies whenever a P-2 episode sweeps by in the local timeseries.

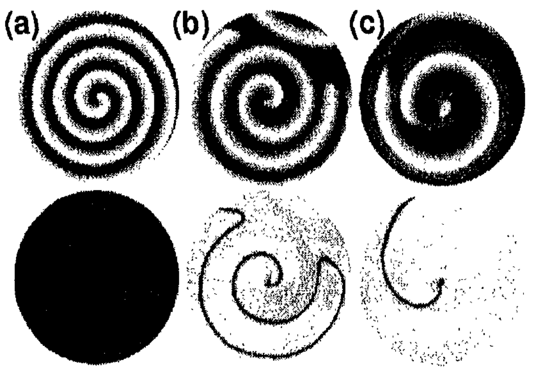

FIG. 3.B.1. Snapshot images of spiral waves (top row) and associated line-defects (bottom row) observed in a BZ reaction-diffusion system: (a) P-1 spiral wave with no line-defect $[H^+]$=3.02 M; (b) continuous P-2 spiral wave and associated line-defect with a shape of P-1 spiral $[H^+]$=2.40M; and (c) discontinuous P-2 spiral and associated line-defect with a shape different from P-1 spiral $[H^+]$=2.12 M. (d) shows two different timeseries (period-1 signal, filled square) and (period-2 signal, filled circle) obtained at A (on the line-defect) and B (not on the line-defect), respectively. The diameter of viewing area is 8.2 mm. The raw images in the first row are obtained using a filtered light (wavelength 480 nm) in a reflective mode. The processed images in the second row visualize a scalar field

$\Delta V(t) = \frac{1}{\tau}\int_0^\tau \left|V(\vec{r},t+t') - V(\vec{r},t+\tau+t')\right|dt'$,where $V(\vec{r},t)$ is the grey value in the raw images. and τ is the period of a fundamental period-1 oscillation. Period-1 domain (i. e. line-defect, $\Delta V = 0$) appears black and period-2 domain appear bright (none zero ΔV). The line-defect in (b) is folded at one side due to an interaction with another line-defect of a neighboring spiral wave (not shown).

When the value of $[H^+]$ becomes smaller, the occurrence of P-2 episode in the local timeseries becomes more frequent and regular [third timeseries in Fig. 3.B.2(a)] and eventually a regular P-2 signal results [fourth timeseries in Fig. 3.B.2(a)]. There is a corresponding change in the line-defect: its breathing motion gradually comes to an end and finally a thin *static* line-defect with the symmetry of a P-1 spiral results as shown in the bottom frame of Fig. 3.B.1(b). The corresponding spiral wave above is thus temporally P-2 but still spatially P-1.[26]

One way to characterize this transition is quantifying the proportion $\rho(t)$ of spatial region executing P-1 oscillation [see Fig. 3.B.2(b)]. The intermittent nature of local timeseries (and breathing motion) is well reflected in the noisy peaks of $\rho(t)$s given for different values of $[H^+]$. The inset of Fig. 3.B.2(b) well illustrates the continuous decreases in the mean value $(\bar{\rho})$ and the standard deviation $(\Delta\rho)$ as $[H^+]$ is lowered. Thus, the transition from the P-1 spiral wave of Fig. 3.B.1(a) to the temporally P-2 (but spatially P-1) spiral wave of Fig. 3.B.1(b) is continuous, in the sense that $\bar{\rho}$ and $\Delta\rho$ both decay continuously.

Interestingly, the described transition has a very strong analogy to the phase synchronization phenomenon generically occurring in systems of two-coupled nonlinear oscillators, which show rare and

---

[26] None of the earlier studies reported such a case. The line-defects of P-2 spiral waves discussed in just decays quadratically in a continuous fashion.

intermittent 2π phase slips near the transition and frequent and regular 2π phase slips away from the transition.[27] The observed P-2 episodes in an otherwise P-1 signal can be considered as 2π slips mediating the transition of a P-1 spiral to a P-2 spiral, or vice versa.

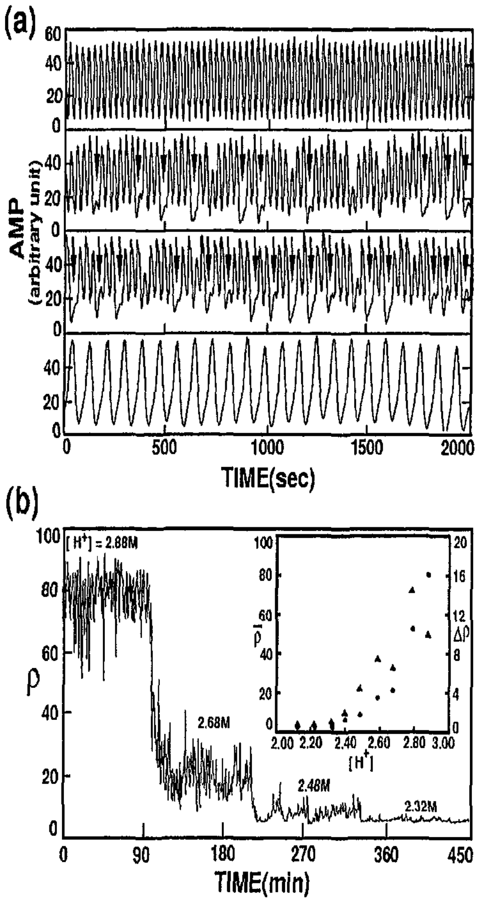

FIG. 3.B.2. Intermittent behaviors during P-1 to P-2 spiral wave transition. (a) Typical local timeseries obtained for different values of $[H^+]$ (from top to bottom, $[H^+]$=3.02 M, 2.80 M, 2.48 M, and 2.12 M). (b) Instantaneous proportion $\rho(t)$ of line-defect for different values of $[H^+]$. The intermittent "P-2 episodes" are marked by arrows in the second and third timeseries of (a). The inset of (b) shows the mean value $\bar{\rho}$ (filled circle) and the standard deviation $\Delta\rho$ (filled triangle) as a function of $[H^+]$. The $\rho(t)$ is evaluated based on a disk area (diameter, 5.3 mm) centered at the spiral core.

When $[H^+]$ becomes about 2.32 M, the static line-defect shown in Fig. 3.B.1(b) is no longer stable and deforms to a different one with a larger pitch [see Fig. 3.B.1(c)]. The pitch of the new line-defect is also larger than that of the corresponding spiral wave as well. Therefore, it cuts through the wave, breaking the continuity of spiral wave. The dynamic process resulting the new line-defect of Fig. 3.B.1(c) is not at all simple as Fig. 3.B.4 illustrates. Following a decrease in $[H^+]$, a complex unwinding process starts more or less from the spiral core region and advances radially outward (t=400). Then, some neighboring line-defects jam into a tight spacing and annihilate each other (t=600), producing two cusp structures (t=700). Subsequently, the cusps travel in opposite directions more or less along the spiral wave profile dilating the pitch (t=1300). The nexus of complex unwinding, annihilation, and dilation process keeps on (t=2400) until a new regular line-defect is established [t=8400 or Fig. 3.B.1(c)].

Although the resulting line-defect is smooth and regular, the ones for the parameter range between Fig. 3.B.1(b) and Fig. 3.B.1(c) are in general quite irregular and unsteady with a complex sequence of unwinding, annihilation, and rewinding

---

[27] M. G. Rosenblum, A. S. Pikovsky, and J. Kurths, Phys. Rev. Lett. **76**, 1084 (1996); U. Parlitz, L. Junge, W. Lauterborn, and L. Kocarev, Phys. Rev. E **54**, 2115 (1996); K. J. Lee, Y. Kwak, and T. K. Lim, Phys. Rev. Lett. **81**, 321 (1998).

processes. Besides, bubble-shaped line-defects and/or irregular patches of breathing line-defects often form spontaneously and interact with the ones associated with spiral waves. All together, a typical morphology of line-defect in this intermediate parameter range can not be distinguished from one of the transient states shown in Fig. 3.B.4. In other words, the shape transition of a line-defect from Fig. 3.B.1(b) to Fig. 3.B.1(c) can not be characterized by a single order parameter like the pitch.

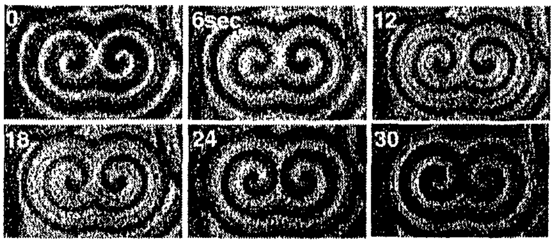

FIG. 3.B.3. Breathing line-defect (black spiraling bands) of a spiral wave pair at P-1 to P-2 transition. The line-defect appears whenever a local P-2 episode [arrows in Fig. 3.B.2(b)] interrupts an otherwise P-1 oscillation. The width of spiraling line-defect changes as a P-2 episode sweeps through in timeseries. The processed images show the scalar field $\Delta V(t)$ The field of view is $8.2 \times 4.8mm^2$ and $[H^+]$=2.80 M.

In contrast to the static line-defect shown in Fig. 3.B.1(b), the line-defect of Fig. 3.B.1(c) is *dynamic* - it rotates steadily like a rigid body in the same direction of spiral wave rotation. However, its rotation is quite slow: roughly 100 times slower than the relevant spiral wave that typically completes one full rotation in an order of 1 minute. The possibility of mode-locking between the shape of spiraling line-defect and that of the relevant spiral wave (i.e., ratio between the relevant two pitches) is investigated in a vicinity of $[H^+]$ =2.22 M to find none. Instead, almost immediately following a small decrease in $[H^+]$, a fascinating meandering transition is observed in the tip dynamics of line-defect as shown in Fig. 3.B.5.

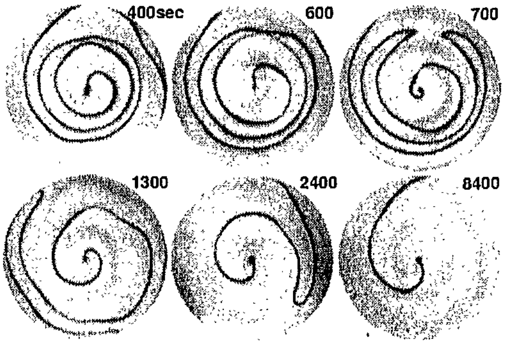

FIG. 3.B.4. Dynamic shape transition of a spiraling line-defect following a decrease in $[H^+]$ (from 2.48 M to 2.22 M at t=0): pitch modulation (t=400); line-defect annihilation and cusps formation (t=600 sec); cusps travelling in opposite directions (t=700-1300 sec); and line-defect acquiring a new smooth profile (t=2400-8400 sec). The processed images show the scalar field $\Delta V(t)$. The diameter of viewing area is 10.6 mm.

An initially simple circular orbit (described by a radius r_1 and a rotation frequency ω_1) [Fig. 3.B.5(a)] undergoes a Hopf bifurcation resulting a compound orbit [Fig. 3.B.5(b)]. The compound orbit formed by two combined circular motions is a hypercloid: the primary circle (radius r_1) orbits the secondary circle (radius r_2) with a new rotation period ω_2 and spins about its center in the same direction. Here, we note that the same ``meandering transition'' is previously observed and extensively analyzed over the last several years in the context of P-1 spiral tip dynamics.[28] It is, however, quite remarkable to observe the same type of transition in relation to a line-defect.

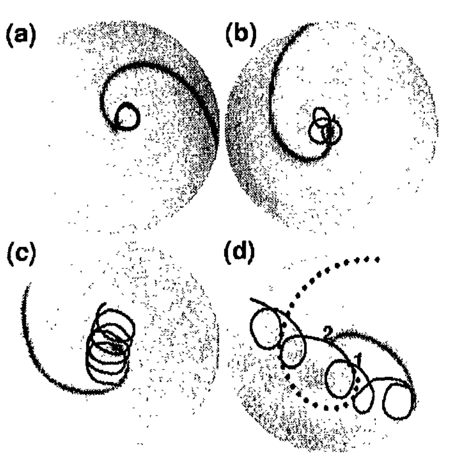

FIG. 3.B.5. Meandering transition and drift of a spiraling line-defect: (a) line-defect having a simple rigid rotation (r_1 = 0.4 mm, ω_1 = 3.8 rad/hr) $[H^+]$ = 2.22 M; (b) meandering line-defect following a hypercloid orbit (r_1 = 0.4 mm, ω_1 = 3.4 rad/hr, r_2 = 0.3 mm, ω_2 = 0.7 rad/hr) $[H^+]$=2.12 M; (c) slow drifting line-defect (r_1 = 0.7 mm, ω_1 = 3.1 rad/hr, r_2 and ω_2 undetermined) $[H^+]$=2.04 M; and (d) fast drifting line-defect (r_1 = 0.8 mm, ω_1 = 5.6 rad/hr, r_2 and ω_2 undetermined) $[H^+]$=1.94 M. The diameter of viewing area is 8.2 mm. All are composite images of a processed line-defect image [$\Delta V(t)$ in grey scale] and the corresponding trajectory followed by its tip (solid line). The dotted line in (d) is drawn to indicate the profile of line-defect at the marked location "1". The line-defect with the maximum (or minimum) curvature reaches at the location "1" (or 2). The rotation frequency Ω of the axxociated spiral wave itself is 594 rad/hr for (a), 552 rad/hr for (b), 528 rad/hr for (c), and 510 rad/hr, respectively.

The shape of compound orbit traced by the tip of line-defect is quite sensitive to the control parameter $[H^+]$. When $[H^+]$ is decreased less then a few percent from that of Fig. 3.B.5(b) r_2 rapidly diverges to infinity and ω_2 becomes very small. Nevertheless, the values of r_1 and ω_1 both change less than 50%. As a consequence, a net drift motion appears as shown in Fig. 3.B.5(c). The drift becomes more eminent when $[H^+]$ is further lowered as shown in Fig. 3.B.5(d). Here, we also note that the shape (or mean curvature) of line-defect is not steady but oscillates periodically as its tip moves on the compound orbit. The line-defect with the maximum (or minimum) curvature reaches at the location marked by "1" (or 2) as indicated in Fig. 3.B.5(d). All these observations are remarkably similar to the ones known for meandering P-1 spiral wave having a compound tip trajectory, except for the fact that no epicycloids are yet observed in our case.[29]

---

[28] D. Barkley, Phys. Rev. Lett. **72**, 164 (1994); G. Li, Q. Ouyang, V. Petrov, and H. L. Swinney, Phys. Rev. Lett. **77**, 2105 (1996); L. Q. Zou, and Q. Ouyang, Phys. Rev. Lett. **85**, 1650 (2000); and S. -M. Hwang, W. G. Choe, and K. J. Lee, Phys. Rev. E **62**, 4799 2000).

[29] Possible existence of epicycloid orbit -- the primary circle orbits the secondary circle in the opposite sense of its self-spinning – is also looked for in our system, in particular in a lower $[H^+]$ regime, but failed. The compound orbit starts significantly being influenced by the system boundary as the pitch of the relevant P-2 spiral becomes comparable to the size of our experimental system. Besides, the image contrast becomes dramatically poor in the lower $[H^+]$ regime.

Section 3.B.4) Discussion

In conclusion, our study clearly demonstrates that line-defects arising in complex periodic media can exhibit highly complex, yet, deterministic dynamics and well defined bifurcations of their own. Full understanding on the observed phenomena, however, would require a derivation of relevant equations of motion for line-defects, which is largely unachieved at this point of time. We also note that the line-defects that we have discussed are all limited to (spiral) traveling waves with a single line-defect attached, and it will be interesting to investigate the same in relation to more complex traveling waves. In addition, it will be also interesting to investigate the existence of such line-defects in systems producing complex periodic standing waves and complex oscillatory biological media (eg. cardiac tissue) as well.

Section 3.C Complex dynamics of a spiral tip in the presence of an extrinsic local modulation

With a generic model excitable system, we have investigated the spatio-temporal dynamics of a simple spiral tip in the presence of an extrinsic *localized* periodic modulation. The tip of the unmodulated spiral traces a circle periodically, while that of the modulated spiral traces a variety of different trajectories depending on the strength and the frequency of the modulation. The modulated motion can be quasi-periodic on a 2-torus, quasi-periodic or partially mode-locked on a 3-torus, or fully chaotic. Various bifurcations including hard Hopf bifurcations and saddle-node bifurcations at strong resonances and period-doubling cascade on a mode-locked 3-torus, are revealed.

Section 3.C.1) Motivation and Background

Rotating spiral waves are ubiquitous in nature and have long elicited the attention of researchers in a variety of different disciplines, including physics,[30] [31] [32] [33] chemistry,[8] [34] [35] and biology.[10]

---

[30] S. Jakubith, H. H. Rotermund, W. Engel, A. von Oertzen, and G. Ertl, Phys. Rev. Lett. **65**, 3013 (1990).
[31] E. Bodenschatz, J. de Bruyn, G. Ahlers, and D. S. Cannell, Phys. Rev. Lett. **67**, 3078 (1991).
[32] K. B. Migler and R. B. Meyer, Phys. Rev. Lett. **66**, 1485 (1991); K. B. Migler and R. B. Meyer, Physica D **71**, 412 (1994).
[33] P. Umbanhowar, F. Melo, and H. L. Swinney, Physica A **1**, 1, (1997).

[36] [37] Among others, of particular interest has been the spatio-temporal dynamics of spiral tip (phase singularity) in excitable or oscillatory media.[38] [39] While the spiral tip dynamics in homogeneous excitable media is now a well explored subject, the effects of extrinsic stimuli on the dynamics of a spiral tip are far less well understood, although they are of great importance.

From the standpoint of physics, the excitable or oscillatory system under external stimuli is a very interesting dynamical system which can result in a variety of rich and complex dynamics. Moreover, understanding the effects of extrinsic stimuli to the natural system would have significant implications in biology. For instance, recent studies on populations of Dictyostelium discoideum show that the dynamics of competition between target waves from pacemaking cells (extrinsic perturbation) and spiral waves in the signaling populations has a significant effect on the morphogenic development of the colony.[40] [41] Also, there might be an important application in cardiology.[10] It is well known that the presence of abnormal cells in the propagation of action potential waves in the heart tissue can result in an abnormally fast heart beat, a deadly heart disease known as tachycardia.[42] Thus, it is essential to understand the physics behind the phenomenon, for example, to develop an ideal strategy for defibrillating stimulus.[43]

---

[31] A. T. Winfree, Science **181**, 937 (1973).
[35] A. N. Zaikin and A. M. Zhabotinsky, Nature **225**, 535 (1970).
[36] K. J. Lee, E. C. Cox, and R. E. Goldstein, Phys. Rev. Lett. **76**, 1174 (1996).
[37] A. T. Winfree, Chaos **1**, 303 (1991).
[38] D. Barkley, Phys. Rev. Lett. **72**, 164 (1994).
[39] G. Li, Q. Ouyang, V. Petrov, and H. L. Swinney, Phys. Rev. Lett. **77**, 2105 (1996), and the references therein.
[40] K. J. Lee, E. C. Cox, and R. E. Goldstein, Phys. Rev. Lett. **76**, 1174 (1996).
[41] K. J. Lee, Phys. Rev. Lett. **79**, 2907 (1997).
[42] D. P. Zipes and J. Jalife, *Cardiac Electrophysiology: From Cell to Bedside* (W. B. Saunders, Philadelphia, 1995).
[43] W. Rappel, F. Fenton, and A. Karma, Phys. Rev. Lett. **83**, 456 (1999).

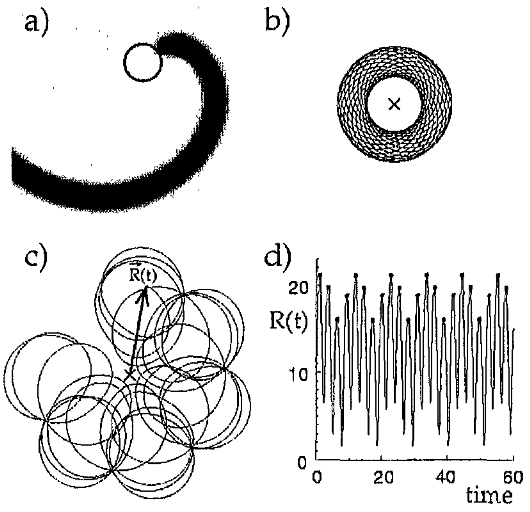

FIG. 3.C.1. The unmodulated (a) and the modulated [(b) and (c)] spiral tip trajectories in two dimensional space, and the timeseries of $R(t)$ corresponding to (c) in (d): $A=0$, $A=0.02$, and $A=0.1$ for (a), (b), and (c), respectively. The origin of the coordinate system was chosen as the site of modulation (marked with "x") and the spiral tip position $\vec{R}(t)$ is defined as the intersection of the two contours $U=0.5$ and $f(U,V)=0$. A snapshot of simple spiral (U-field, 96×96 domain) is shown in (a) together with its circular tip trajectory. The modulation frequency f_m is fixed at 0.37. While (b) and (c) are to scale, (a) is not to scale with (b) and (c).

Here, we investigate the spatio-temporal dynamics of a spiral tip in the presence of a localized extrinsic periodic modulation (i.e., like a pacemaker periodically perturbing the system). The modulated tip dynamics can be very complex in both space and time, exhibiting phenomena of entrainment, mode-locking, multi-stability, and period-doubling cascade that leads to chaos. Our system differs from those of the earlier studies[44] [45] [46] [47] which focus on the effects of spatially homogeneous modulations. In particular, our study is complementary to the recent work by Petrov *et al.*[46] who have studied resonant patterns in an oscillatory system with global periodic modulation in presence. To the best of our knowledge, a recent study by Rappel *et al.*[48] is the only report that addresses the effects of localized modulation. This study focuses on the feasibility of using a discrete set of stimuli for controlling the undesirable wave instability that can occur in a set of equations modeling dynamics of cardiac tissue.

Section 3.C.2) Method

Our study is based on the following two species model:

---

[44] O. Steinbock, V. Zykov, and S. C. Müller, Nature **366**, 322 (1993).

[45] A. P. Muñuzuri, M. Gómez-Gesteira, V. Pérez-Muñuzuri, V. I. Krinsky, and V. Pérez-villar, Phys. Rev. E **50**, 4258 (1994).

[46] V. Petrov, Q. Ouyang, and H. L. Swinney, Nature **388**, 655 (1997); A. Lin *et al.*, "Resonant Pattern Formation in a Spatially Extended Chemical System", in *Pattern Formation in Continuous and Coupled Systems* (Springer, New York, 1999), eds. M. Golubitsky, D. Luss, S. H. Strogatz.

[47] D. M. Goldschmidt, V. S. Zykov, and S. C. Müller, Phys. Rev. Lett. **80**, 5220 (1998).

[48] W. Rappel, F. Fenton, and A. Karma, Phys. Rev. Lett. **83**, 456 (1999).

$$\frac{\partial U}{\partial t} = F(U,V) + \nabla^2 U,$$

$$\frac{\partial U}{\partial t} = F(U,V) + \nabla^2 V + M(x_0, y_0, t; A, f_m),$$

where $F(U,V) = \in^{-1} U(1-U)\{U-(V+b)/a\}$ and $G(U,V) = U - V$ are the kinetic function and $M(x_0, y_0, t; A, f_m)$ models a localized periodic modulation. $\in, a$, b are the system parameters. Except for the modulation term, the set of equations is a generic two-species reaction-diffusion model proposed earlier by Barkley.[49] The Barkley model is well known, not only for its efficiency in computation, but also for its faithful representation of many essential features of excitable systems. The locally modulated reaction-diffusion model is computed numerically.[50]

Section 3.C.3) Results

Figure 3.C.1 illustrates three different types of orbits traced by a spiral tip, following a continuous increase in A.[51] Initially, a particular set of system parameters ($\in = 0.005, a = 0.33, b = 0.01$) is chosen to produce a simple spiral whose tip rotates steadily along a circle with a natural frequency f_0=0.387931 and radius r_0=7.06; see Fig. 3.C.1(a). Upon increasing A for a fixed value of f_m, fixed, the simply periodic tip becomes unstable, moves gradually toward the modulation site, then stabilizes to execute a quasi-periodic motion following a hypocycloid - a compound orbit of two circular motions, where the primary circle (radius r_1) orbits the secondary circle (radius r_2) with frequency f_2 and spins about its center in the same direction with frequency f_1[52]; see Fig. 3.C.1(b). The rotation frequency f_1 along the primary circle is locked to the modulation frequency f_m. For all hypocycloid orbits that we have examined, there is no evidence of mode-locking as in the earlier studies

---

[49] D. Barkley, M. Kness, L. S. Tuckerman, Phys. Rev. A **42**, 2489 (1990).

[50] Explicit Euler method is used for a 200 × 200 square-grid with no-flux boundary condition. The diffusion terms are evaluated by finite difference 9-point formula after computing the reaction terms. The grid size and the temporal step size are Δx=0.16 and Δt=0.005, respectively. Throughout this Letter, the distences are given in units of Δx and the time is given in units of 200 Δt.

[51] We focus on the dynamics and bifurcations of a spiral tip by varying A for a few different fixed values of f_m that are close to but smaller than the natural frequency of the unmodulated spiral. When $f_m > f_0$, the spiral tip is gradually repelled away from the modulation site, as discussed.

[52] The primary circle is actually a slightly squished circle (i.e., an ellipse) as discussed in [49].

on unmodulated systems.[3,8]

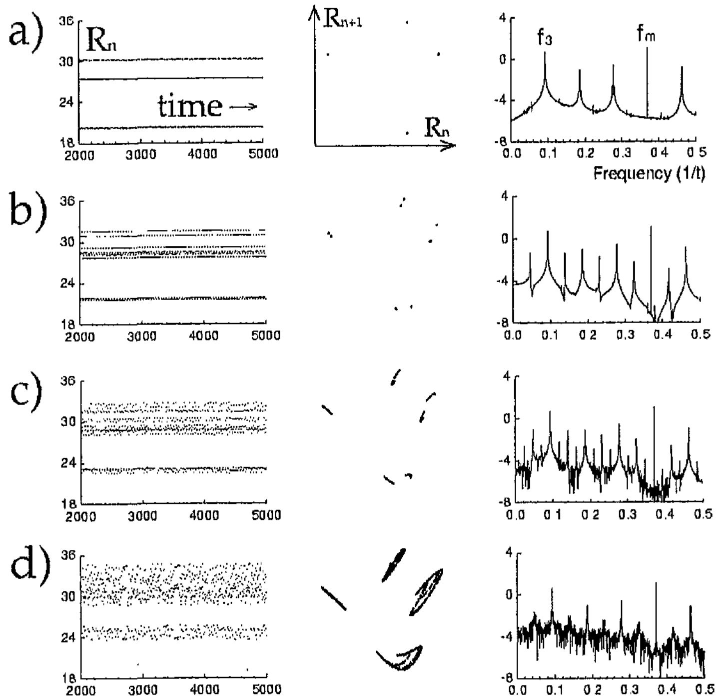

FIG. 3.C.2. Mode locking and period-doubling cascade of R_n with increasing value of A: (a) 1:4 resonance (P4), A=0.1, (b) period-doubled 1:4 resonance ($P8$), A=0.5, (c) twice-doubled 1:4 resonance ($P16$), A=0.57, and (d) chaotic state, A=0.8. The first, the second, and the third column respectively shows timeseries of local maxima R_n of $R(t)$, return maps of R_n, and power spectra of $R(t)$. A fixed value of f_m=0.37 is given in $\log_{10}$ scale.

With a further increase in A, the hypocycloid orbit again becomes unstable to form a more complex compound orbit around the modulation site; see Fig. 3.C.1(c). The dynamics on this orbit can be better understood by investigating the time evolution of $R(t)$, the distance between the modulation site and the position of the tip, since it removes one rotational degree of freedom associated with the secondary circular orbit (r_2, f_2). The timeseries of R in Fig. 3.C.1(d) shows a composite oscillation with two different frequencies f_1 and f_3, where f_3 is a new frequency independent of f_1 and f_2. Thus, we conclude that the complex compound orbit in Fig. 3.C.1(c) consists of three circular motions that lie on a 3-torus. The example shown in Fig. 3.C.1(c) is in particular a resonant state with f_3: f_1=1:4. The 1:4 resonance is clear in the timeseries of local maxima R_n, the return map of R_n, and the power spectrum of $R(t)$ in Fig. 3.C.2(a). The bifurcation from the quasi-periodic 2-torus [Fig. 3.C.1(b)] to the resonant state [Fig. 3.C.1(c)] is studied in a greater detail and is found to be a saddle-node bifurcation immediately following a hard Hopf bifurcation to 3-torus; the transition is hysteretic with a small but finite region of bistability, as shown in the inset of Fig. 3.C.3. Although f_3 locks to f_1, f_2 does not lock to f_1 in a rational fraction, thus, the resonant orbit is a particular one on a 3-torus with a partial mode-locking.

Beyond the 1:4 resonant 3-torus state, we also find a period-doubling cascade. Somewhere between A=0.415 and A=0.42, the four resonant lines (in R_n), four points (in return map of R_n), and peaks (in the power spectrum of $R(t)$) in Fig. 3.C.2(a) all double to form a period-doubled 1:4 resonant state [Fig. 3.C.2(b)]. When A is further increased, the period-doubled 1:4 resonant state becomes unstable, again doubling to form the twice-doubled 1:4 resonant state as shown in Fig. 3.C.2(c). Subsequent cascade of period doubling ultimately leads to a chaotic state shown in Fig. 3.C.2(d). The bifurcation diagram shown in Fig. 3.C.3 summarizes the hysteretic transition and the period-doubling cascade.

Besides the subharmonic resonant states of 1:4 mode-locking, other various resonant states also occur with a smaller value of f_m as shown in Fig. 3.C.4. In addition to the two primary resonances of 1:3 and 1:4, one secondary resonance 2:7=(1+1:3+4), three tertiary resonances 3:10=(1+2:3+7), 3:11=(2+1:7+4), 3:13=(1+2:4+9), and three fourth-order resonances 4:13=(1+3:3+10), 4:15=(3+1:11+4), 4:17=(1+3:4+13) are evident, and a few higher order resonance states are also confirmed, although not presented in the Figure. The resonant states all together form a devil's staircase as in the well known case of circle map. The question of the completeness of the staircase of Fig. 3.C.4 remains open due to the limits on our computational capability.

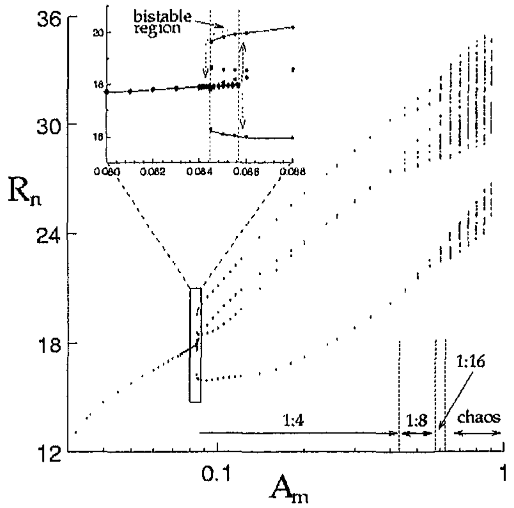

FIG. 3.C.3. Bifurcation diagram showing hysteretic transition to 1:4 resonance and period-doubling cascade. The inset figure shows the detail of the hysteresis at the onset of the 1:4 resonant state on a 3-torus. With increasing A (filled diamond) the transition occurs at about A=0.0854 and with decreasing A (filled circle) the transition back to a 2-torus occurs at smaller value of about A=0.0845.

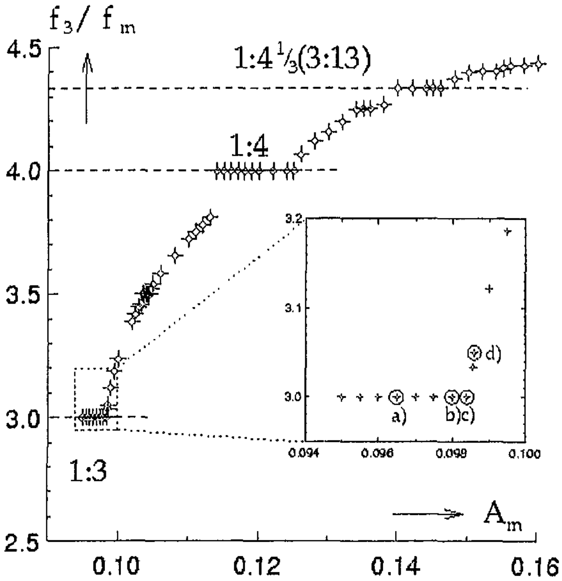

FIG. 3.C.4. Various resonant states shown in f_3 / f_m vs A plot. The resonant states with $f_m/f_3 = 3, 3\frac{1}{4}, 3\frac{1}{3}, 3\frac{1}{2}, 3\frac{2}{3}, 3\frac{3}{4}, 4, 4\frac{1}{4}$, and $4\frac{1}{3}$ are evident. The resonant (nonresonant) states are marked with filled circles (empty triangles). A fixed value of f_m=0.355 is used. The inset illustrates the complex bifurcation sequence showing the breakup of the 1:3 resonant state (discussed in the text).

The bifurcations between resonant states and nearby non-resonant states are in general very complex. A detailed bifurcation sequence in the vicinity of the 1:3 resonant state in particular is shown in the inset of Fig. 3.C.4; and Fig. 3.C.5 shows some representative phase portraits along the bifurcation sequence. The dashed line in the inset corresponds to the stable quasi-periodic attractor on a 2-torus, the dotted line to the resonant attractor on a 3-torus, and the solid line to the nonresonant attractor on a 3-torus. In the return maps of Fig. 3.C.5, the quasi-periodic attractor on a 2-torus appears as a fixed point [the center dot in Fig. 3.C.5(a)-(e)], the 1:3 resonant state as a period-3 cycle [Fig. 3.C.5(b) and (c)], and the nonresonant attractor on a 3-torus as a limit cycle [Fig. 3.C.5(e) and (f)]. For parameter values between the points 1 and 3, and between 4 and 5, the system is bistable.

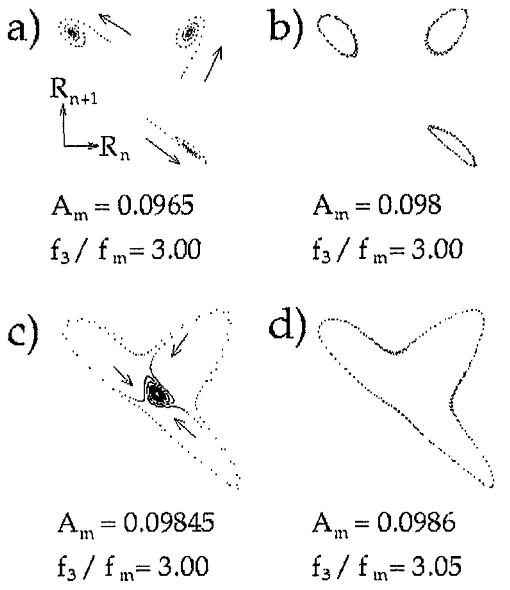

FIG. 3.C.5. Return maps of R_n along the bifurcation sequence shown in the inset of Fig. 4. With increasing sequence of A, (a) quasi-periodic state on a 2-torus (A=0.0920 – before 1); (b) f_3: f_1 =1:3 resonant state on a 3-torus (A=0.0955 -- between 1 and 2); (c) f_3:f_1 =1:3 resonant state on a 4-torus (A=0.0980 – between 2 and 3); (d) quasi-periodic state on a 2-torus (A=0.0985 – between 3 and 4); (e) quasi-periodic state on a 3-torus (A=0.0986 – between 4 and 5); and (f) quasi-periodic state on a 3-torus (A=0.0995 – after 5). Note that (b), (c), and (e) are bistable. In the map of (d), some transient flow is included to visualize the "ghost" loop. The arrows indicate the directions of flow.

The fixed point in Fig. 3.C.5(a) is stable and globally attracting below point 1. At point 1, a stable period-3 cycle is born via a saddle-node bifurcation [Fig. 3.C.5(b)]. Subsequently, the three elements in the period-3 cycle become unstable via a Hopf bifurcation at point 2, forming small limit cycles around each element of the period-3 cycle [Fig. 3.C.5(c)]. The corresponding tip dynamics thus takes place on a 4-torus with an additional frequency f_4 with f_3 still mode-locked with f_1. The attractor on 4-torus loses stability again at point 3 to return to the quasi-periodic state on a 2-torus [Fig. 3.C.5(d)]. At point 4, a pair of limit cycle (one stable and the other unstable) is created [Fig. 3.C.5(e)]. The unstable limit cycle shrinks toward the fixed point and disappears via subcritical Hopf bifurcation at point 5, beyond which only the nonresonant limit cycle is stable and globally attracting [Fig. 3.C.5(f)]. The transitions at points 4 and 5 are the characteristics of a hard Hopf bifurcation.

Hysteretic transitions are also observed near the onset of other resonance states, but they can be quite different from that of 1:3 resonant state. For instance, the hysteretic transition at the left end of 1:4 resonance in Fig. 3.C.4 is caused by the competition between a resonant and a nonresonant attractors on a 3-torus. Below the point I, only a nonresonant limit cycle is stable and globally attracting. At point I, a periodic-4 cycle is created just outside the nonresonant limit cycle via a saddle-node bifurcation. At point II, the nonresonant limit cycle then disappears, colliding with another unstable limit cycle.

Beyond the point II, the system is completely resonant.

Section 3.C.4) Discussion

In summary, we have investigated the dynamics of a spiral tip under a localized extrinsic periodic modulation and found a wealth of complex attracting states: (1) for small values of A, the tip executes quasi-periodic motions on a 2-torus with no indication of mode locking; (2) for intermediate values of A, the tip either executes a quasi-periodic motions with three incommensurate frequencies or partially mode-locked motions on a 3-torus; and (3) for large values of A, the tip motion ultimately becomes chaotic. Various bifurcations on a 2-torus leading to partially mode-locked states on a 3-torus; (2) cascade of period-doubling bifurcations leading to the chaotic motion; and (3) multi-stability between various attracting orbits.

In the future, resonant states for different modulation frequencies will be explored for a complete phase digram showing the structure of Arnold's tongues. The potential applications of the result in biological systems will be also investigated. Finally, we suggest a relatively simple experiment to confirm our results. One can use the well known excitable BZ reaction with light-sensitive catalyst such as Ruthenium-bipyridil complex[44-46] in a continuously-fed reactor; the localized sinusoidal modulation can be given by a tightly focused laser beam whose intensity is modulated in time.

Section 3.D Superlattice, Rhombus, Square, and Hexagonal Standing Waves in magnetically driven ferrofluid surface

Standing wave patterns that arise on the surface of ferrofluids by (single frequency) parametric forcing with an ac magnetic field are investigated experimentally. Depending on the frequency and amplitude of the forcing, the system exhibits various patterns including a superlattice and subharmonic rhombuses as well as conventional harmonic hexagons and subharmonic squares. The superlattice arises in a bicritical situation where harmonic and subharmonic modes collide. The rhombic pattern arises due to the non-monotonic dispersion relation of a ferrofluid.

Section 3.D.1) Motivation and Background

The phenomena of self-organization in spatially extended nonequilibrium systems have attracted much attention lately in the scientific community world-wide. Various controlled experiments are developed to study different pattern forming mechanisms and bifurcations among different patterns.[53] One of the latest scientific issues in this regard is to investigate the system in which a finite number of unstable (spatial or temporal) modes interact each other, while the past studies have mostly focussed on the limiting cases of either pattern forming systems where a single spatial mode is excited or systems that are highly turbulent with many spatial and temporal modes.

Such issue was first raised in a experiment of parametrically driven surface waves: Edwards and Fauve used a two-frequency excitation scheme and were able to generate a quasi-crystalline standing wave pattern with 12-fold symmetry.[54] In subsequent experiments on a similar experimental setup, Kudrolli *et al.* observed two different types of superlattice pattern (“type-I'” and “‘type-II”) in addition to the 12-fold symmetric quasi-crystalline pattern.[55] More recently, Arbell and Fineberg report yet another kinds of superlattice pattern (“SSS” and “2MS”).[56] All these unusual patterns are obtained in two-frequency forced Faraday experiments in which two *externally* excited modes interact (i. e. near bicriticality). Very recently, however, Wagner *et al.* have demonstrated that such bicritical condition can be achieved even by a single frequency forcing for a viscoelastic liquid[57] or for a normal Newtonian fluid in an extreme driving condition (very shallow filling depth and large shaking elevations).[58] New types of superlattice pattern are revealed in those systems. The existence of these unusual patterns all together suggests a large class of previously unanticipated spatio-temporal patterns with multiply interacting modes.

Section 3.D.2) Method

Here, we take a step in this direction by experimental study on a vertically oscillating ferrofluid

---

[53] See, e.g., M. Cross and P. Hohenberg, Rev. Mod. Phys. **65**, 851 (1993).
[54] W. S. Edwards and S. Fauve, J. Fluid Mech. **278**, 123 (1994); Phys. Rev. E **47**, R788 (1993).
[55] A. Kudrolli, B. Pier, and J. P. Gollub, Physica D **123**, 99 (1998).
[56] H. Arbell and J. Fineberg, Phys. Rev. Lett. **81**, 4384 (1998).
[57] C. Wagner, H. W. Müller, and K. Knorr, Phys. Rev. Lett. **83**, 308 (1999).
[58] C. Wagner, H. W. Müller, and K. Knorr, "Crossover from a square to a hexagonal pattern in Faraday surface waves", patt-

that is driven by a sinusoidal magnetic field. There are two reasons for choosing the new system over previously investigated ones.

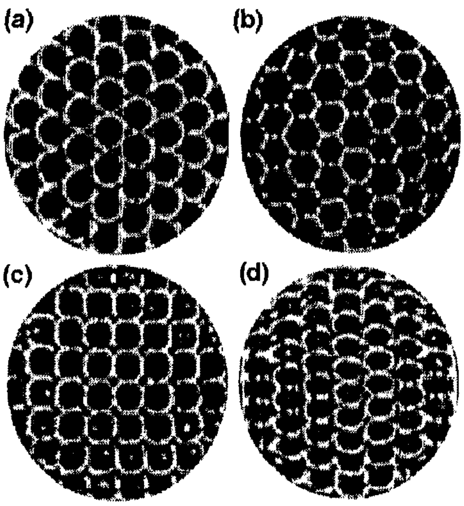

FIG. 3.D.1. Regular patterns observed on the surface of a driven ferrofluid in a cylindrical container: (a) harmonic hexagon (f = 6.0 Hz), (b) subharmonic superlattice (f = 6.7 Hz), (c) subharmonic square (f = 11.0 Hz), and (d) subharmonic rhombus (f = 20.0 Hz). The total magnetic field is $H(t) = H_0 + \Delta H \sin(2\pi f t)$, where H_0/H_c and $\Delta H/H_c$ are fixed at 0.94 and 0.22, respectively. The diameter of the viewing area is 60 mm.

First of all, the driven ferrofluid system can be easily brought near to a bicritical situation with a single frequency forcing - the harmonic mode as well as subharmonic mode can be generated by an ac magnetic field with a small driving frequency (<30 Hz) and a small magnetic field (<100 G).[59] [60] This contrasts with the case of mechanically driven Newtonian fluids in which either a complex two-frequency forcing scheme or an extreme driving condition is necessary to achieve a bicritical situation.[61]

The other reason is that ferrofluid exposed to a magnetic field can exhibit a non-monotonic dispersion relation.[62] Due to the non-monotonicity the neural stability curve for the excitation of standing waves can have multiple minima,[63] [64] thus, several spatial modes can be excited simultaneously - an ideal situation for studying pattern formation in which a finite number of unstable modes interact.

Section 3.D.3) Results

As expected, the driven ferrofluid system is quite rich to reveal a variety of standing wave patterns as shown in Fig. 3.D.1. Two unusual patterns, (1) superlattice with a mixed-mode oscillation

---

sol/9911001 (1999).

[59] J. -C. Bacri, U. d'Ortona, and D. Salin, Phys. Rev. Lett. **67**, 50 (1991).

[60] T. Mahr and I. Rehberg, Europhys. Lett. **43**, 23 (1998).

[61] H. Müller, H. Wittmer, C. Wagner, J. Albers, K. Knorr, Phys. Rev. Lett. **78**, 2357 (1997).

[62] R. Rosenweig, *Ferrohydrodynamics*, Cambridge University Press, Cambridge (1985).

[63] D. Raitt and H. Riecke, Phys. Rev. E **55**, 5448 (1997).

[64] T. Mahr and I. Rehberg, Phys. Rev. Lett. **81**, 89 (1998).

and (2) subharmonic rhombic pattern, as well as usual subharmonic square and harmonic hexagonal patterns are observed. The observed superlattice is similar but different from any of the previously observed ones in its shape and temporal evolution. The rhombic pattern is the first example of its kind ever demonstrated in experiments on nonequilibrium pattern formation. In the following, we describe our experimental setup, present a detailed bifurcation/phase diagram, and discuss the underlying pattern forming mechanisms.

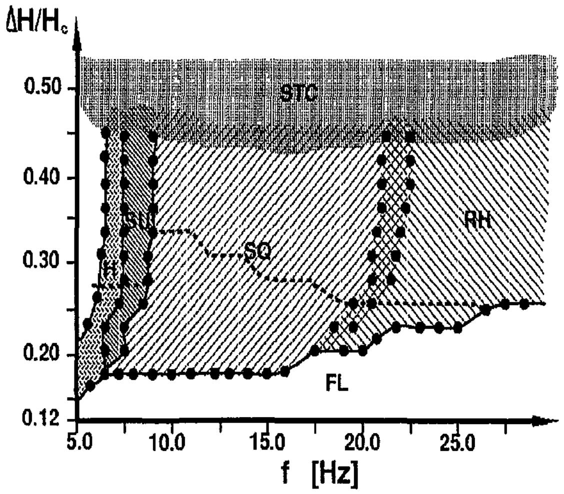

FIG. 3.D.2. Phase diagram of standing wave patterns revealed in a magnetically driven ferrofluid with $H_0 = 0.94H_C$: flat surface (FL), hexagon (H), superlattice (SU), square (SQ), and rhombus (RH). The thin shaded area between SQ and RH is bistable (i. e. SQ and RH coexist). Spatio-temporal chaotic state (STC) is generally observed at large ΔH. Crossing the dashed line toward the STC state, the crystalline states start to acquire defects.

The ferrofluid is a colloidal suspension of magnetic powder stabilized by screened electrostatic repulsion.[6 5] We use a commercially available ferrofluid (EMG901, Ferrofluidics) [density $\rho = 1.53$ g/ml, surface tension $\sigma = 29.5$ g/s^2, initial magnetic susceptibility $\chi = 3.00$, magnetic saturation $M_s = 600$ G, dynamic viscosity $\eta = 10$ cp, yielding a critical field of the static Rosensweig-instability $H_c = 79.73$ G]. A cylindrical Teflon container containing the ferrofluid (depth = 5 mm, diameter = 85 mm) is placed in the center of a pair of Helmholtz-coils (Cenco instruments) with a inner (outer) diameter of 100 mm (300 mm). The magnetic field is monitored by means of a hall probe (F. W. Bell Inc., Model 4048), and the spatial variation of the field strength from the center to the outer rim is within 3%. An ac signal is generated from a home-built synthesizer-board and amplified by a linear amplifier driving the total magnetic field of $H(t) = H_0 + \Delta H \sin(2\pi f t)$. H_0 is the static field, ΔH is the amplitude of ac component, and f is the driving frequency. H_0 is fixed at $0.94\ H_c$ for all cases, while ΔH and f are used as a control

---

[6 5] M. Silber and M. R. E. Proctor, Phys. Rev. Lett. **81**, 2450 (1998); M. Silber and A. C. Skeldon, Phys. Rev. E **59**, 5446 (1999).

parameter.

The fluid surface is illuminated by two arrays of concentric LED rings (diameter 100 mm and 120 mm, respectively) located 230 mm above the surface. The flat surfaces either above or below the level of the surrounding fluid appear white, while the non-flat surfaces that scatter the light away from the camera appear black. The current lighting method is sufficient to verify the spatial structure and distinguish the temporal response (harmonic or subharmonic). The patterns are imaged using a high speed 256 × 256 pixel CCD camera (Dalsa, CA-D6-0256W) located 370 mm above the surface with a fast frame grabber (Matrox, Meteor-II). Maximum frame acquisition rate is 955 frame/s, enabling us to photograph distinct phases of moving pattern.

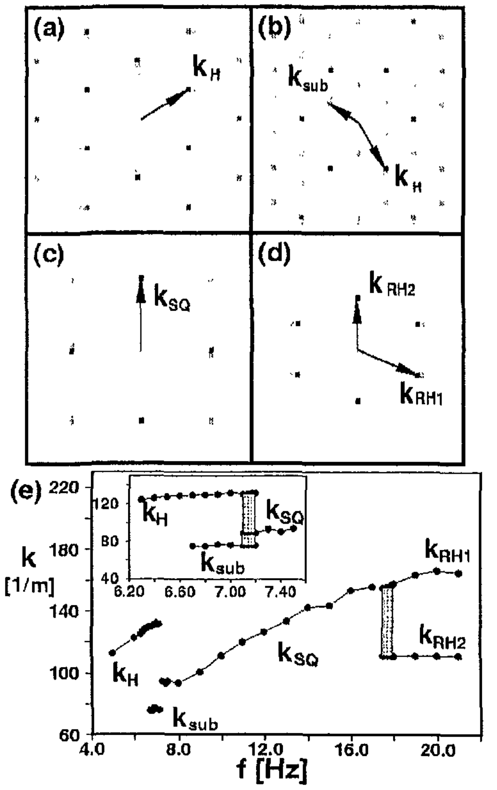

FIG. 3.D.3. Fourier transforms of the regular patterns shown in Fig. 3.D.1: (a) hexagon, (b) superlattice, (c) square, and (d) rhombus. The magnitude of wavevectors associated with different patterns vs f are shown in (e). The insets shows the details of the transition among hexagon, superlattice, and square.

A phase diagram is presented in Fig. 3.D.2. Upon increasing sequence of ΔH, the flat surface can be unstable to various crystalline states depending on the value of driving frequency f. Squares and rhombuses occur over a wide range of parameter space, whereas hexagons and superlattice form only in a narrow range at low driving frequency. Spatio-temporal chaotic state (STC) gradually forms with increasing number of defects as ΔH increases. Essentially, the same phase diagram is obtained with a square container. In other words, the observed patterns are insensitive to the symmetry of the container.

We first focus on the sequence of bifurcations that occur with increasing value of f for a fixed value of $\Delta H / H_c = 0.22$. The flat fluid surface becomes unstable first to a harmonic mode for a small f. Since the up-down symmetry is broken for a harmonic mode, quadratic interaction is the most significant nonlinearity,[53] producing hexagonal standing wave pattern that is synchronous to the ac driving [Figs. 3.D.1(a) and 3.D.3(a)]. With a gradual increase in *f*, the wave number (k_H) increases slightly [see Fig. 3.D.3(e)] but the hexagonal symmetry does not change until *f*=6.7 Hz at which the system enters into the bicritical region. At the onset of bicriticality, 6 subharmonic peaks $(k_{sub} = k_h / \sqrt{3})$ suddenly appear forming a superlattice pattern together with the primary 6 harmonic peaks [see Figs. 3.D.1(b) and Fig. 3.D.3(b)]. The transition is first order and non-hysteretic within the accuracy of our experiment, although we can not exclude the possibility of a small region of bistability.

The observed superlattice pattern is similar but different from the ones previously observed by others.[55] [56] [57] [58] In particular, the snap shot of superlattice [Fig. 3.D.4(a)] taken at $t = 0$ is basically tiled by three different cells differing in sizes and shapes. During one driving cycle the cell "M" returns to the same "M", while "S" and "L" swap each other. Upon completing the subsequent driving cycle, "M" returns to the same, but "S" and "L" swap again. In other words, the superlattice in Fig. 3.D.1(b) has a mixed mode oscillation. This is in marked contrast with the purely subharmonic hexagonal superlattices observed by Wagner *et al.* that alternates between two complementary hexagonal lattices composed with cells of same type,[57] and also with the "Type-II superlattice" observed by Kudrolli *et al.* that undergoes a complex stripe modulation during the course of oscillation.[55]

The superlattice forms in a narrow region between harmonic hexagon and subharmonic square. It is thus natural to believe that the superlattice forms as a result of an interplay between the two different modes with different spatial and temporal symmetries. The resulting pattern is not likely to be a mere superposition of the two. Instead, nonlinear interactions between them would generate new modes. Since both harmonic and subharmonic modes are present, dominant nonlinearity of inter-mode interection is quadratic, generating new subharmonic modes. Translational invariance also requires the newly generated wavevectors are linear combinations of k_H and k_{SQ}. These new wavevectors would in turn interact with the dominant harmonic hexagonal basis, and only those which satisfy the (spatial and temporal) resonance conditions would survive.[65] Two out of four subharmonic square modes k_{SQ} and four out of new subharmonic modes satisfy the resonance conditions, and form a hexagonal sublattice with magnitude $(k_{sub} = k_h / \sqrt{3})$, thus contributing to the superlattice. The present mechanism for the generation of the superlattice is very similar to that of.[5 8] The difference in the cell sizes ("S", "M", and "L") of the observed superlattice is due to the difference in the strength of the involved modes.

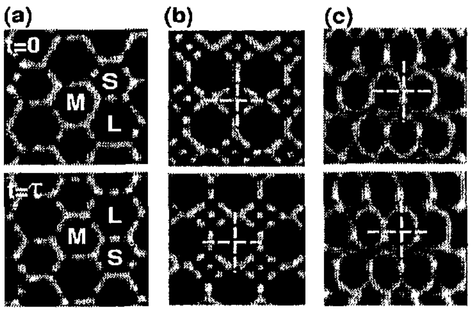

FIG. 3.D.4. Time evolution of subharmonic patterns during one driving cycle: (a) superlattice, (b) square, and (c) rhombus. The patterns after one driving period (τ) are shown in the bottom row. The dashed cross lines are placed to indicated the same location.

As f is increased further, the superlattice undergoes a hysteretic transition to a subharmonic square lattice; upon increasing (decreasing) sequence of f, the superlattice (square) transforms to the square (superlattice) at $f = 7.10$ Hz ($f = 7.20$ Hz). In the bistable regime, mixed states of square domains and superlattice domains are often seen. At the transition to the square pattern, k_{SQ} is approximately $k_h / \sqrt{2}$. The properties of the observed square pattern are identical to the ones of square lattices that are usually observed in conventional Faraday experiments: the pattern alternates between two dual square lattices as shown in Fig. 3.D.4(b) at every driving period. The k_{SQ} increases significantly as f increases.

Upon increasing f further, the system undergoes another hysteretic transition to a stable rhombic pattern with a well defined 2-fold symmetry [see Figs. 3.D.1(d) and Fig. 3.D.3(e)]. At the transition, k_{SQ} branch continues to k_{Rh1} (primary rhombic basis vectors) and a new basis vector k_{Rh2} that is the difference between two neighboring k_{Rh1}s is spontaneously created. The oblique angle between k_{Rh1} and k_{Rh2} characterizes a particular rhombic pattern. For the example shown in Fig. 3.D.3(d), $k_{\mathrm{Rh2}}/k_{\mathrm{Rh1}} = 0.696$ and the angle between the two neighboring basis wave vectors is 69.7° The oblique angle changes but only slightly as the driving frequency changes (less than 2% for the frequency range 17.5 - 21.0 Hz). The system is bistable for for the range ($17.5 < f < 18.0$ Hz). Except for the bistable region, the rhombic lattice is globally stable. Fig. 3.D.4(c) clearly demonstrate that the observed rhombic pattern is temporally subharmonic just as the square pattern shown in Fig. 3.D.4(b). As far as we know, the observed rhombic pattern is the first laboratory demonstration of its kind ever revealed.[66]

At this point, we note that a recent theoretical study has shown that parametrically driven surface waves on ferrofluids can be unstable to multiple spatial modes simultaneously.[63] Here, the existence of multiple unstable modes originates from the non-monotonic dispersion relation of ferrofluids. The study has shown that in one-dimensional geometry one can realize a situation that different domains with different wavevectors coexist. Such phenomenon is also verified recently in an experiment conducted in a quasi one-dimensional annular geometry.[64] The existence of rhombic pattern in our system, however, suggests that in two-dimensional space the (two) unstable modes rather form a deformed crystalline structure (i. e. rhombic lattice), instead of domains with different wavevectors. In our experiments, coexisting domains with different wavevectors are only observed in bistable regions. In order to check the feasibility of this hypothesis, we have extended the earlier theoretical study by Raitt and Riecke[63] to two-dimensional space and have found a parameter regime in which well defined rhombic patterns are stable.[67] Recently, Lifshitz and Petrich have also demonstrated the existence of a stable rhombic pattern in a generic model system ("two-mode Swift-Hohenberg" equation) containing two unstable spatial modes.[68]

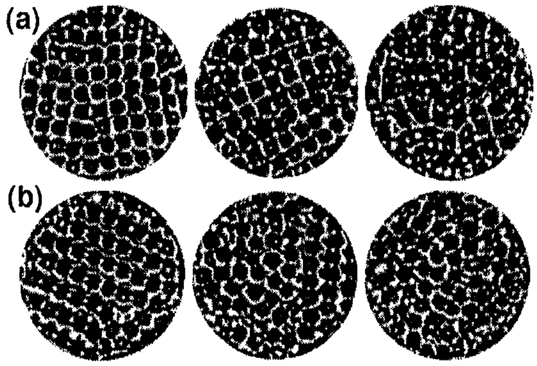

FIG 3.D.5..Transitions to disordered patterns from (a) square and (b) rhombus, as ΔH increases. The frequency f is fixed at 15.0 Hz for (a) and 21.0 Hz for (b). $\Delta H/H_c$ is 0.28, 0.39, and 0.45 (from left to right) for (a), and 0.28, 0.37, 0.45 for (b).

In the following, the transition to spatio-temporal chaotic state (STC, see Fig. 3.D.2) from

---

[66] Experimental evidence of stable rhombic pattern was discussed earlier in a chemical reaction-diffusion system by Q. Ouyang *et. al.* [Chaos **3**, 707 (1993)]. However, their observation is markedly different from ours: their rhombic lattice has a broad spectrum of angles with a mean value of 60°, whereas our rhombic lattice is essentially tiled by a single rhombus with an oblique angle far different from 60°.

[67] Amplitude equations for a non-monotonic dispersion relation are constructed in two dimensional space, then investigated numerically with a pseudo-spectral method. We find stable rhombic pattern as well as stable square pattern. More details on this study will be published elsewhere.

[68] R. Lifshitz and D. M. Petrich, Phys. Rev. Lett. **79**, 1261 (1997).

crystalline states is qualitatively described. As ΔH increases for a fixed value of f, the crystalline patterns gradually become disordered. Figure 3.D.5 shows two such sequences, one for the case of square and the other for the case of rhombic pattern. Dislocations and defects start to form in a square lattice near ΔH / H_c = 0.28 [Fig. 3.D.5(a), left image]. As ΔH increases, the number of defects increases (middle image) and eventually the whole lattice becomes very loose as in a typical melting process. The last image in Fig. 3.D.5(a) shows a state very near to STC, showing a very little trace of square lattice. A similar melting process is also observed for the case of rhombic lattice [Fig. 3.D.5(b)]. The gradual deformation toward the state of STC is not limited to the square and rhombus but occurs in the whole range of f that we have explored. This observation is consistent with the earlier Faraday experiments conducted with Newtonian fluids.[69] [70]

Section 3.D.4) Discussion

In conclusion, superlattice and rhombus, as well as square and hexagonal standing waves, are observed on the surface of ferrofluids driven parametrically with an ac magnetic field. The superlattice pattern forms in a narrow bicritical region between harmonic hexagonal lattice and subharmonic square lattice. It is argued that the superlattice pattern is formed by the resonance of newly generated subharmonic modes with the harmonic hexagonal mode already present. Due to the non-monotonic dispersion relation of the ferrofluids, multiple spatial modes can become unstable simultaneously with a single frequency forcing. As a consequence, stable rhombic patterns are possible and observed in the experiment. Full understanding of the observed patterns and their mutual boundaries, however, pose quite a challenge. Different crystalline patterns revealed in this study are all obtained with a fixed value of dc field ($H_0 < H_c$). It would be also interesting to investigate patterns that would arise when ($H_0 > H_c$). i.e. in the supercritical regime where the base surface pattern is a static hexagonal (or square) lattice, instead of a flat surface.

Section 3.E Successive spatial period-doublings in magnetically driven ferrofluid surface

---

[69] N. Tufillaro, R. Ramshankar and J. Gollub, Phys. Rev. Lett. **62**, 422 (1989).
[70] A. Kudrolli and J. P. Gollub, Physica D **97**, 133 (1996).

Superlattice standing waves that arise on the surface of ferrofluids driven by an ac magnetic field are investigated experimentally. Several different types are obtained by successive spatial period-doublings that are mediated by resonant mode interactions. The observed superlattices are quite diverse, depending on relevant base modes, the orientation and number of emerged subharmonic modes, and the phase difference among the involved Fourier modes all together. On the other hand, their temporal evolutions are all either period-1 (harmonic) or period-2 (subharmonic), in a good contrast with complex periodic traveling waves recently observed in complex
oscillatory media.

Section 3.E.1) Motivation and Background

Pattern formation in spatially extended nonequilibrium system has been a subject of numerous studies during the last decade. Various laboratory and model systems are developed and characterized in different scientific disciplines.[53] Among others, perhaps the most important concern in these efforts has been to understand "simple crystalline patterns" that arise due to a single mode instability. This is now a well established topic. Subsequently, an immediate question one might ask is if there are any generic routes along which the morphological complexity of a simple pattern increases in a systematic way. Much of the current research effort related to nonequilibrium pattern formation now lies on this venue of thought.

In many cases, one can view pattern forming nonequilibrium systems as a coupled network of nonlinear oscillators. Then, the morphological complexity of pattern is closely related to the temporal dynamics of the constituent oscillators. For instance, a series of recent model studies and laboratory experiments on different reaction-diffusion systems has shown that a subharmonic bifurcation of local oscillators in time domain can lead to a spatially period-doubled traveling wave state.[71] [72] [73] [74] A number of such subharmonic bifurcations then can result a highly complex yet periodic patterns. In a different class of systems, however, such complex patterns can be induced not by the complexity of local

---

[71] A. Goryachev and R. Kapral, Phys. Rev. Lett. **76**, 1619 (1996).
[72] A. Goryachev, H. Chaté and R. Kapral, Phys. Rev. Lett. **80**, 873 (1998).
[73] A. Goryachev, H. Chaté and R. Kapral, Phys. Rev. Lett. **83**, 1878 (1999).
[74] J.-S. Park and K. J. Lee, Phys. Rev. Lett. {\bf 83}, 5393 (1999).

dynamics but rather by resonant mode interactions. Pattern forming nonlinear systems are often able to generate different spatial modes simultaneously, and resonant interactions among these base modes can result various spatially complex-period lattice (superlattice) pattern. This different class of patterns is a subject of extensive current investigations.[54] [56] [55] [57] [58] [75] [76]

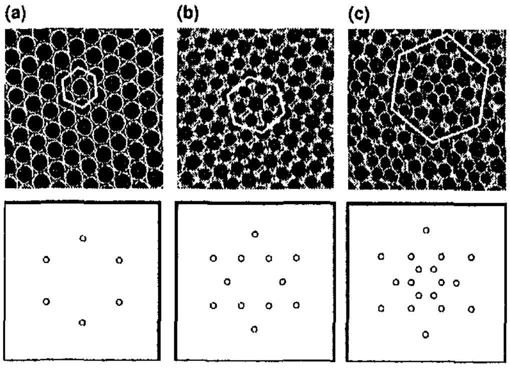

FIG. 3.E.1 Successive spatial period doublings of a hexagonal lattice: (a) harmonic hexagon 1*h* (f = 6.20 Hz, $\Delta H = 0.17H_c$); (b) spatially period-2 harmonic superlattice 2*h* (f = 5.60 Hz, $\Delta H = 0.50\ H_c$); and (c) spatially period-4 subharmonic superlattice 4*H* (f = 6.06 Hz, $\Delta H = 0.42H_c$) are shown at the top row. H_c(=108.0 gauss) is the critical field of static Rosensweig instability of the 1:1 mixture. Each frame is $61 \times 61 mm^2$. Each hexagonal tiling units are guided by white line. The *corresponding Fourier modes are shown at the* bottom row.

Here, we demonstrate that successive spatial period-doublings can arise in a system with nonlinear resonant interactions as shown in the example of Fig. 3.E.1. With a resonant mode interaction, subharmonic modes associated with the initial base wavevectors appear and render a spatially period-doubled lattice. As the control parameters are varied further, a spatial period-doubling takes place again with an additional subharmonic bifurcation. As it will be demonstrated, the morphology of the resulting superlattice can be quite diverse depending on the involved base wavevectors, the orientation and number of the emerged subharmonic modes, and the phase difference among the selected Fourier modes. However, the temporal dynamics of the all observed superlattices are either harmonic or subharmonic unlike the case of complex oscillatory media, in which the spatial and temporal complexities increase or decrease simultaneously.

Section 3.E.2) Method

The patterns are observed in a magnetically driven Faraday system employing ferrofluids.[59]

---

[75] H. Arbell and J. Fineberg, Phys. Rev. Lett. **84**, 654 (2000).

[76] H. Arbell and J. Fineberg, Phys. Rev. Lett. **85**, 756 (2000).

[77] [78] Ferrofluids are colloidal suspension of magnetic powder stabilized by screened electrostatic repulsion.[62] Unless specified otherwise, 1:1 mixture of commercially available ferrofluids (EMG901 and EMG909, Ferrofluidics) is used.[79] A cylindrical Teflon container containing the ferrofluid (fluid depth = 1.16 mm. container depth = 50 mm, inner diameter = 140 mm) is placed in the center of a pair of Helmholtz coils with an inner (outer) diameter of 200 mm (280 mm). The distance between two coils is 120 mm. The magnetic field is monitored by a hall probe (F. W. Bell Inc., Model 6010), and the spatial variation of the field strength is within 3% in the monitored area. An ac signal is generated from a home-built synthesizer-board and amplified by a linear amplifier driving the total magnetic field of $H(t)=H_0+\Delta H \sin(2\pi ft)$. H_0 is the static field, ΔH is the amplitude of ac component, and f is the driving frequency. H_0 is fixed at 0.93 H_c for all cases, while ΔH and f are used as control parameters. The temperature of the container is maintained at 15°C.

The fluid surface is illuminated by three arrays of concentric LED rings (diameter 160, 180 and 200 mm, respectively) located 275 mm above the surface. The patterns are imaged at a resolution of 530×512 pixels using a charged coupled device (CCD) camera (Quantix, Photometrics) located 560 mm above the surface with a frame grabber (Meteor2/DIG, Metrox) in stroboscopic modes with an exposure time of 3 ms. The flat surfaces either above or below the level of surrounding fluid appear white, while the non-flat surfaces that scatter the light away from the camera appear black.

Section 3.E.3) Results

A good example of successive spatial period-doublings is shown in Fig. 3.E.1. Figure 3.E.1(a) shows a temporally harmonic hexagonal standing wave pattern (1*h*) and the associated six wavevectors. This pattern, which usually forms in a vicinity of Rosensweig (static) instability, is simply periodic both in space and time. As the driving amplitude and frequency are increased, however, the 1*h* pattern

---

[77] T. Mahr and I. Rehberg, Europhys. Lett. **43**, 23 (1998).

[78] H.-J. Pi, S.-y. Park, J. Lee, and K. J. Lee, Phys. Rev. Lett. **84**, 5316 (2000).

[79] The physical properties of EMG901 (EMG909) are, density ρ = 1.53 (1.02) gm/ml, surface tension σ = 27.5 (27.5) g/s^2, initial magnetic susceptibility χ = 3.00 (0.80), magneti saturation M_s = 600 (200) gauss, dynamic viscosity η = 10 (6) cp, yielding a critical field of static Rosensweig instability 90.5 (168.2) gauss, respectively.

undergoes a subharmonic bifurcation resulting a spatially ``period-2" hexagonal superlattice (2*h*) as shown in Fig. 3.E.1(b).

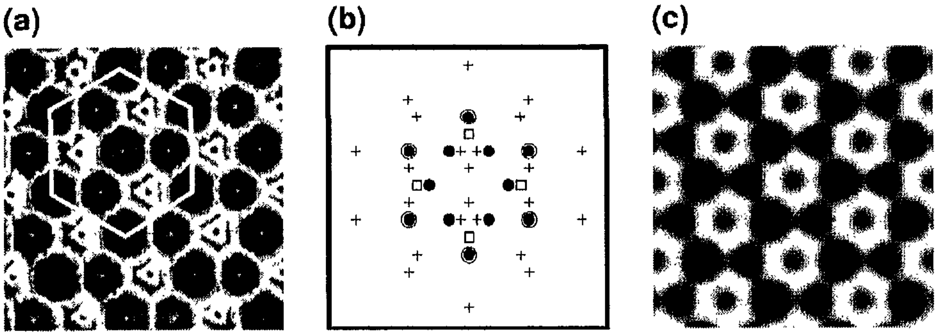

FIG. 3.E.2 Generation of 2*H* hexagonal superlattice by resonant triadal interaction: (a) snapshot of 2*H* pattern (f = 8.00 Hz, $\Delta H = 0.25H_c$, field of view=44 x 44 *mm*^{2}), (b) twelve modes of 2*H* (•, measured from (a) directly), six harmonic hexagonal modes of 1*h* (○, obtained from a measured dispersion relation), four subharmonic square modes of $1S_1$ (□, obtained from a measured dispersion relation), and modes generated by triadal interactions (+) between 1h and 1 S_1, and (c) Reconstructed image based on the measured twelve modes. Basic hexagonal tiling unit is guided by white line in (a).

The magnitude of the newly emerged six subharmonic wavevectors, which are rotated 30° relative to the six base modes, are exactly $\sqrt{3}$ times smaller than the original base wavevectors. The 2*h* pattern is still harmonic in time. As the driving frequency increases, the 2*h* superlattice undergoes another subharmonic bifurcation in space [see Fig. 3.E.1(c)] - a set of six secondary subharmonic modes appears in addition to the base modes and the six primary subharmonics, thus forming a spatially "period-4" hexagonal superlattice (4*H*). Unlike the case of the first subharmonic bifurcation, the secondary subharmonic wavevectors are 2 times smaller than those of the primary subharmonics, lining up with the primary subharmonics. The 4*H* superlattice is temporally subharmonic. The underlying mechanism for the observed spatial period-doublings is far different from that of complex oscillatory media - here, resonant mode interactions are responsible for the observed phenomenon.[6 5 7 8]

Let us first discuss simple resonant triadal interaction resulting a hexagonal superlattice pattern 2*H* shown in Fig. 3.E.2(a). The 2*H* is observed in a ``small amplitude regime" whereas the 2*h* and 4*H* are seen in a "large amplitude regime." The 2*H* clearly originates from a resonant triadal interplay between harmonic hexagonal modes of 1*h* and subharmonic square modes of $1S_1$ (due to conventional Faraday instability, see.[7 4] As shown in Fig. 3.E.2(b), of total 12 relevant modes of 2*H* (black filled dots), outer 6 and inner 2 modes (along the horizontal line) originate from the base modes of 1*h* (open circle) and $1S_l$ (open square), respectively, and the remaining inner 4 modes originate from the resonant modes (+) of triadal interactions between $1h$ and $1S_l$. The $2H$ pattern thus has a subharmonic oscillation in time as a whole. The existence of three different cell sizes is simply a result of π/2 phase difference between the harmonic and subharmonic modes as demonstrated in the reproduced image of Fig. 3.E.2(c).

Although the Fourier spectra of $2H$ and $2h$ are identical, they are different in two aspects: (1) $2H$ is subharmonic in time, while $2h$ is harmonic; and (2) the six subharmonic Fourier peaks of $2h$ pattern can not be obtained by simple triadal interaction of $1h$ and $1S_l$ modes. These differences together naturally lead us to conclude that the $2h$ pattern does not arise by simple resonant triadal interaction but by resonant interaction with a higher order. Also, the fact that $2h$ pattern has a simple harmonic oscillation excludes any possible connections to higher order resonant tongues (e.g. $3f/2$ tongue). The observed $4H$ pattern can be only explained with higher order resonant interaction as well with a similar reasoning. Indeed, the $2h$ and $4H$ patterns are only observed in a large amplitude regime in which high (higher than the triadal) order resonant interactions become important.

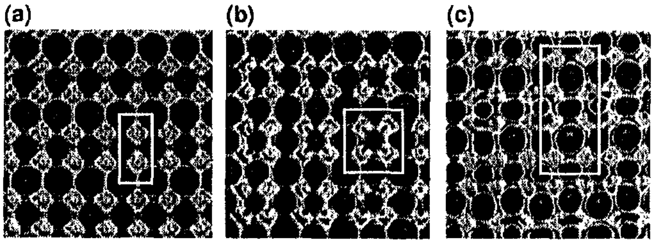

FIG. 3.E.3. Successive spatial period doublings of a square lattice. The simple subharmonic square $1S_l$ (not shown) bifurcates to either (a) spatially period-2 *anisotropic* square $2S_a$ (f = 6.52 Hz, $\Delta H = 0.3H_c$) or (b) spatially period-2 *isotropic* square $2S_i$ (f = 7.00 Hz, $\Delta H = 0.30H_c$). (c) The $2S_i$ superlattice further bifurcates to spatially period-4 {\it anisotropic} square $4S_a$ (f = 7.00 Hz, $\Delta H = 0.29H_c$). Each frame is 44 × 44 mm^2. Each square (or rectangular) tiling units are guided by white line.

Similar spatial period-doubling phenomena are also observed in a square lattice as well. Figure 3 shows three different square superlattices $2S_a$, $2S_i$, and $4S_a$ formed by resonant mode interactions. The temporally subharmonic square standing wave $1S_l$ undergoes a spatial period-doubling to either $2S_a$ [Fig. 3.E.3(a)] or $2S_i$ [Fig. 3.E.3(b)], as the system is brought in a large amplitude regime. Only a pair of subharmonic wavevectors newly appears along one of the two symmetric axises of the pre-existing four base vectors for *anisotropic* $2S_a$, while two pairs of subharmonics appear simultaneously for *isotropic* $2S_i$. Consequently, $2S_a$ is spatially period-doubled only in one direction (y-axis for the given example), whereas $2S_i$ is doubled in both x and y directions. The transition between two eighboring states $2S_a$ and $2S_i$ is found to be continuous. In other words, the additional pair of subharmonic modes along k_x axis gradually appears from $2S_a$ pattern rendering $2S_i$ pattern, as the driving frequency or amplitude is increased.[8]

When the system is moved further from $2S_i$ to a higher frequency regime, an additional doubling occurs resulting the $4S_a$ pattern shown in Fig. 3.E.3(c). The complex square superlattice $4S_a$ has total ten Fourier modes including four base vectors of $1S_1$, four primary subharmonics of $2S_i$, and a new pair of secondary subharmonics along one of the two principal axises. This additional pair is exactly half the size of the pre-existing primary subharmonics. Thus, the $x-y$ symmetry is lost in $4S_a$ as in the case of $2S_a$. In the current experimental condition, no isotropic
$4S$ superlattice has been found.

Careful analysis on the Fourier modes of all three square superlattices $2S_a$, $2S_i$, and $4S_a$ has been carried out in conjunction with all possible triadal resonant interactions between the modes of two basic lattices $1h$ and $1S_1$, which are measured from a dispersion relation curve obtained in our experiment. The agreements between the observed and the predicted modes generated by triadal mode interactions turn out to be poor for the primary subharmonics of $2S_a$ and $2S_i$, and worse for the secondary subharmonics of $4S_a$. In other words, it is quite unlikely that these square based superlattices originate from triadal interactions, although we can not completely rule out such a possibility.

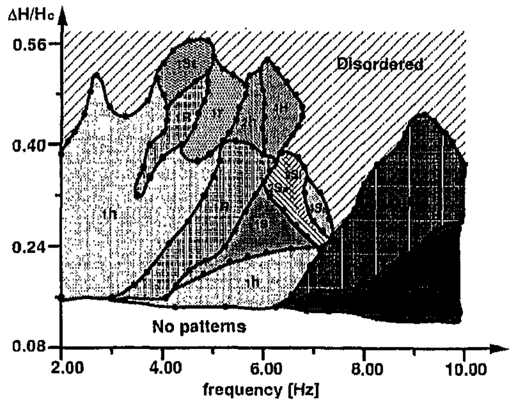

FIG. 3.E.4. Phase diagram of standing wave patterns revealed in a magnetically driven ferrofluid with $H_0 = 0.93H_c$. All together, six different superlattices ($2h$, 2H, 4H, $2S_i$, $2S_a$, $4S_a$) and six different simple lattices ($1h$, $1s$, $1S_1$, $1S_2$, $1r$, $1R$) are observed. The following labelling convention is used throughout the paper: the numerics (1, 2, or 4) and the following letters (h & H=hexagon, s & S=square, r & R=rhombus) specify the spatial periodicity and the relevant lattice symmetry, respectively. The small (capital) letters mean temporally harmonic (subharmonic). The additional subscripts are i=*isotropic*, a=*anisotropic*, 1=first kind, and 2=second kind, respectively.

The spatial periodicity of four is the highest thus achieved so far, but in principle the doubling cascade can go on further as the number of modes participating the resonant interaction increases. On

---

[8] Since the acquired full image is not sufficiently large to reveal the subharmonic Fourier peaks clearly, we quantified this transition by directly measuring the ratio (m) of two different cell sizes along the x-axis. The order parameter m decays continuously from $2S_i$ to $2S_a$. The driving frequency f is varied while maintaining $\Delta H = 0.30\ H_C$.

the contrary, some of high order resonant mode interactions can produce simple lattice patterns as well. A good such example is the subharmonic square lattice $1S_2$ observed in a large amplitude regime. Although it is identical to the $1S_1$ pattern in all aspects, their Fourier modes have a quite different origin - none of its four wavevectors match to the wavevectors of $1h$, $1S_1$, or the ones created by triadal interactions between them. This is also true for the harmonic rhombus $1r$ also observed in a large amplitude regime.

The phase diagram shown in Fig. 3.E.4 well summarizes the rich variety of observed patterns and their relative locations - all together, *twelve* different types are revealed. In addition to the ones discussed earlier, simple harmonic square lattice $1s$ and subharmonic rhombus $1R$ are also observed in a small amplitude regime. The $1R$ forms with conventional triadal interaction.[81] The $1s$ pattern neighboring $1h$ is very similar to the ones discussed in previous reports.[55,75] The transitions between two neighboring patterns are all hysteretic[82] except for the one between $2S_a$ and $2S_b$, which is continuous as described earlier.

The overall structure of the phase diagram depends quite sensitively on the property of the used ferrofluid. For a comparison, we have conducted the same experiment with 2:1 mixture of EMG901 and EMG909 to find no superlattice what so ever, and with EMG901 only to find a superlattice of $2H$ type. Nevertheless, the two basic competing lattices, $1h$ and $1S_1$, both are present in all three different cases. In other words, the two primary instabilities are not so sensitive to the property of the fluid, but the resonant mode interactions are.

Section 3.E.4) Discussion

In summary, we have investigated superlattice standing wave patterns that arise on the surface of parametrically driven ferrofluids. All together, six different superlattices along with six different simple lattices are observed. It is significant that all of the observed superlattice arise through spatial period-doublings mediated by resonant mode interactions. A similar spatial period-doubling

---

[81] Our 1R pattern has the same origin of the ``two-mode rhomboid" ($2kR$) pattern described in[75] except that all four Fourier modes of 1R pattern are resonant modes whereas only two out of four are such for the $2kR$ pattern.

[82] The bistable ranges are typically an order of $f = 0.1\text{Hz}$ and $\delta\left[\frac{\Delta H}{H_c}\right] = 0.02$.

phenomenon is reported earlier in the context of traveling waves of complex oscillatory media, but it is discussed for the first time in the context of standing waves and resonant mode interaction. All of the observed superlattices are temporally simple (either harmonic or subharmonic to the forcing), in a good contrast to the complex periodic traveling waves which are complex oscillatory in time as well. Our experimental results raise a number of important new issues such as (1) why the subharmonic modes of the base wavevectors are so much preferred by resonant interactions over other possibilities, and (2) what would be the maximum spatial complexity that can be achieved by resonant mode interaction under a given condition. Full understanding on the rich variety of standing wave patterns and their mutual boundaries also pose quite a challenge.

Section 3.F Fabrication of micro-stamp and patterned cell network

Elastomeric stamps with micrometer-sized grids are fabricated for building biological cell networks by design. Polymerizing polydimethyl-siloxane (PDMS) stamps are cast in a variety of different molds prepared by micro-electro mechanical systems (MEMS) technology. Micro square grid patterns of 3-aminopropyl triethoxy silane (APS) are successfully imprinted on glass plates and patterned networks of cardiac cells are obtained as designed. The resulting cellular networks clearly demonstrate that the cell attachment and growth are greatly favored on the APS treated thin tracks. Here we report the technical details related to the fabrication of microstamps, stamping procedure, and the culture method. The potential applications of patterned cellular network are also discussed.

Section 3.F.1) Motivation and Background

Development of a proper tool for measuring electrical signals of living cells has brought a host of important understandings in such areas as neurosciences and cell biology. Single channel recording device like the *patch-clamp* is now a standard and essential tool in any neurosciences laboratories world-wide. In the mean time, as the personal computer (PC) technology has progressed significantly over the last few decades, a huge amount of data can be easily acquired and handled routinely using a PC, and it is thus now possible to record signals associated with hundreds of cells simultaneously. Incidently, developing a proper multi-channel recording device has become an up-to-date issue in bio-engineering community.[83] At the same time demands on multi-channel recording device are great in neurosciences community as the recent understandings on biological neural networks are in a large part based on spatio-temporal activities of the relevant networks.

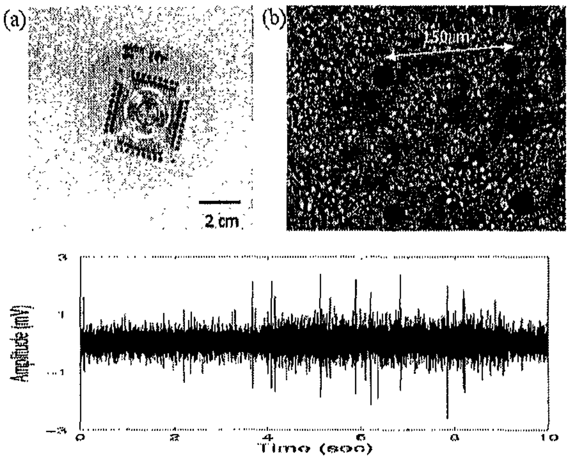

FIG. 3.F.1. 64-channel multi-electrode array (MEA) plate with a culture-ring attached (a), cerebellar neuronal culture on a MEA plate (b), and a typical neuronal spike time series acquired through one of the electrode (c).

One latest research effort for the understanding of spatio-temporal dynamics of electrically active biological cell network is using a multi-electrode array (MEA) plate in conjunction with cell culture as shown in Fig. 3.F.1.[84] This multi-channel recording device is fabricated recently in our laboratory using micro-electro mechanical systems (MEMS) technology. Figure 3.F.1(a) shows a 64-channel MEA plate with a "culture-ring" attached, and Fig. 3.F.1(b) shows a close-up view of a complex cell network grown on the top of the MEA plate. Our complete system involves a MEA culture plate, neuronal culture, 64-channel amplifying system electronics, and 4-channel stimulators (not shown). This particular system is developed to understand the generic properties of biological neural network such as possible determinism embedded in spike timeseries data generated by the individual cells and the correlations or information flows among neighboring cells. It turns out, however, the desired analysis is still hindered by the morphological complexity of the cultured network. As Fig. 3.F.1(c) well illustrates, a typical spike signal acquired through a single micro-electrode is often a mixture of several different signals generated by a group of neurons that are located around the particular electrode. Various spike sorting algorithms have been applied to separate the individual signals out from the mixed choir but mostly unsuccessful due to the fact that the amplitude and shape of the spikes

---

[83] Macro Bove, Massimo Grattarola, Sergio Martinoia and Giovanni Verreschi "Interfacing cultured neurons to planar substrate microelectrodes: characterization of the neuron-to-microelectrode junction," Bio-electrochemistry and Bio-energetics 38, pp. 255-265 (1995)

[84] L. J. Breckenridge, R. J. A. Connolly and C. D. W. Wilkinson, "Advantages of using microfabricated extracellular electrodes for

generated even by a single neuron vary as it moves during the course of signal measurement. Several different excitable cells are employed as well but the signal sorting problem still remains as a big challenge.

This technical difficulty naturally has lead us to develope a more simplified cell network that is better defined than the one shown in Fig. 3.F.1(b). In achieving this goal, we recently fabricated various elastomeric stamps with micrometer-sized features for the use in guided cellular network growth. Here we report the technical details for fabricating these stamps, discuss the selected chemicals used for micro-pattern imprinting, and characterize the physical properties of the imprinted patterns using a lateral force microscope (LFM) and an atomic force microscope (AFM). Finally, we show some of our preliminary examples of patterned cellular network as guided by the imprinted micro-patterns. The cellular network patterning or the differential cell attachment is rendered possible by the differential cytophilicity of the involved cells to the different chemicals imprinted on the substrate.

Section 3.F.2) Method

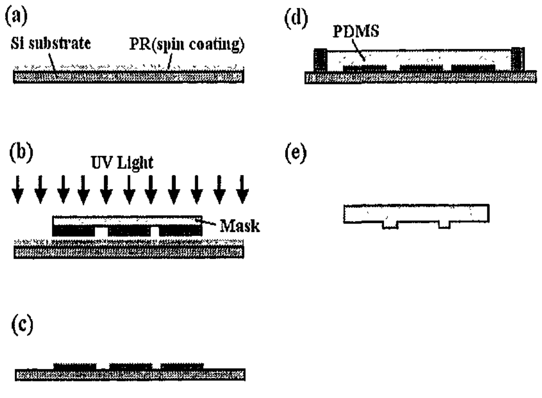

FIG. 3.F.2. Microstamp fabrication procedure: (a) 2 µm PR spin-coating on Si substrate and softbake; (b) UV light exposure (12 mW, 7.5 sec); (c) photoresist development and hardbake; (d) PDMS pouring and curing; and (e) final PDMS micro-stamp.

In order to achieve a well defined simple network, we recently developed a method using micro-stamps that are fabricated by polymerizing polydimethyl-siloxane (PDMS). The PDMS stamps are cast in a finely etched mold that is prepared by MEMS technology. The whole microstamp fabrication process is well illustrated in Fig. 3.F.2 and similar procedures are also described in [85] [86] [87] First, AZ1512 photoresist (PR) is spin-

---

in vitro neuronal recording," J. Neurosci. Res., Vol. 42, pp. 266-276 (1995.)

[85] D. W. Branch, B. C. Wheeler, G. J. Brewer and D.E. Leckband, "Long-Term Maintenance of Patterns of Hippocampal Pyramidal Cells on Substrates of Polyethylene Glycol and Microstamped Polylysine," IEEE Trans. Biomedical Engineering, Vol. 47, No. 3, March (2000)

coated on a 4-inch Si wafer and softbaked at 95 ℃ [Fig. 3.F.2(a)]. Through a patterned mask ultraviolet(UV) light is exposed to the wafer [Fig. 3.F.2(b)]. After a conventional developing and hardbaking step, the fine grid patterns of PR become a desired mold [Fig. 3.F.2(c)]. Then, various PDMS microstamps are cast using a 1:10 (v/v) mixture of Sylgard silicon and Sylgard silicone elastomer 184 (Dow Corning Inc.). The mixture is poured into the prepared PR mold and cured at room temperature [Fig. 3.F.2(d)]. Finally, the cured PDMS is lifted carefully from the mold and a final PDMS microstamp is ready for stamping [Fig. 3.F.2(e)].

A proper set of physical dimensions associated with PDMS stamp is quite critical for successful imprinting of chemicals and subsequent guided cell network growth. We find that the thickness of the PR pattern is ideal to be 2㎛ as suggested by Kumar and Whitesides in an earlier report.[8 8] When the relief of a microstamp is longer than the ideal, coating materials such as APS would not easily disengage from the stamp intaglio off onto the glass slide that is to be patterned. The PR thickness is controlled by adjusting the rotation speed of spin-coater.

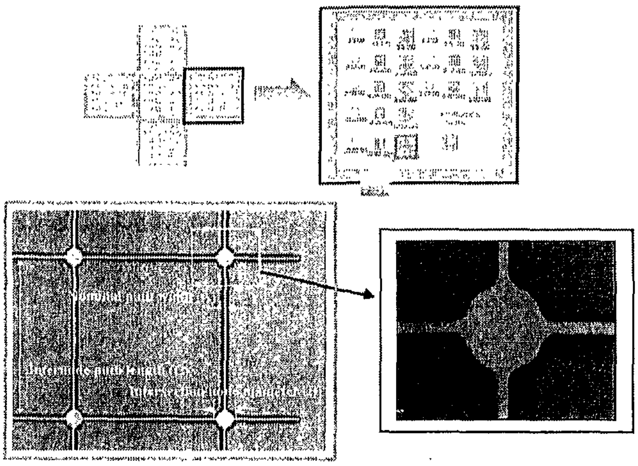

FIG. 3.F.3. Entire mask layout (full wafer) and successive close-up views of a fabricated mold. All 24 different square grid patterns are fabricated on a single wafer. The physical dimension A, B, C of the shown example is 5, 20, and 160, respectively. The two grey scale images at the bottom are optical images in a transmission mode.

Various square grid patterns (in x-y plane) are designed with a careful consideration on the actual dimensions of the cell body including extra details like neuritis. The patterns are basically a mesh

---

[8 6] J. M. Corey, A. L. Brunette, M. S. Chen, J. A. Weyhenmeyer, G., J. Brewer and B. C. Wheeler, "Differentiated B104 neuroblastoma cells are a high-resolution assay for micropatterned substrate," *Journal of Neuroscience Methods*, Vol. 75, pp. 91-97 (1997)

[8 7] N. S. Seong, S. M. Hwang, K. J. Lee, D. J. Ahn and J. Pak, "Fabrication and experiment of microstamp for neuron patterning," the 8th Korean Conference on Semiconductors, pp. 665-666 (2001)

[8 8] Amit Kumar and Georage M. Whitesides, "Patterned Condensation Figures as Optical Diffraction Gratings," Science, vol. 263, pp. 60-62, January (1994).

of square grids with circular nodes at the intersections (see Fig. 3.F.3). Twenty four different variations of the basic square grid patterns are designed by varying the internode path length (80, 120, and 160 μm), circular node diameter (5, 10, and 20 μm), and width of the thin track (3, 5, and 10 μm), and all are fabricated simultaneously on a single wafer.

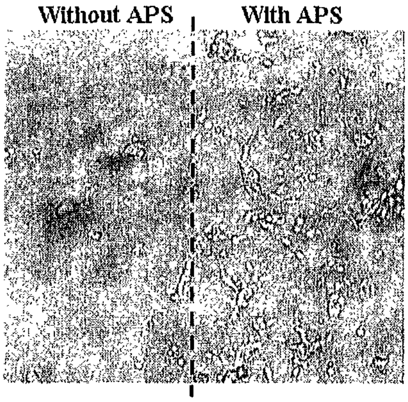

FIG. 3.F.4. Cerebellar granule cell culture showing a preferential cell attachment (cytophilicity) the APS coated region.

FIG. 3.F.5 LFM image of an imprinted APS pattern (focussed at a single intersection, A=10, B=20, and C=120, all in μm).

A differential cytophilicity of cells to the different chemicals imprinted on the substrate is a key ingredient for a successful cell network patterning and growth. Typically, biological cells prefer to adhere to a hydrophilic surface, and a conventional biological cell culture experiment employs a substrate coated with such a material as poly-D-lysine. Therefore, one can in principle design any morphology of cultured cell network by employing a differential patterning of a hydrophilic coating material with a hydrophobic one. Recently, we found that neurons and cardiac cells both have a good cytophilicity to the chemical known as APS. As Fig. 3.F.4 demonstrates clearly, cells very much prefer to attach themselves to the region where APS is coated. Homogeneously distributed cell populations at initial stage migrate toward the coated region, and those left out on the untreated region eventually die and being washed out when the culture medium is replenished. This observation lead us to use APS as a imprinting chemical for guided cell network growth.

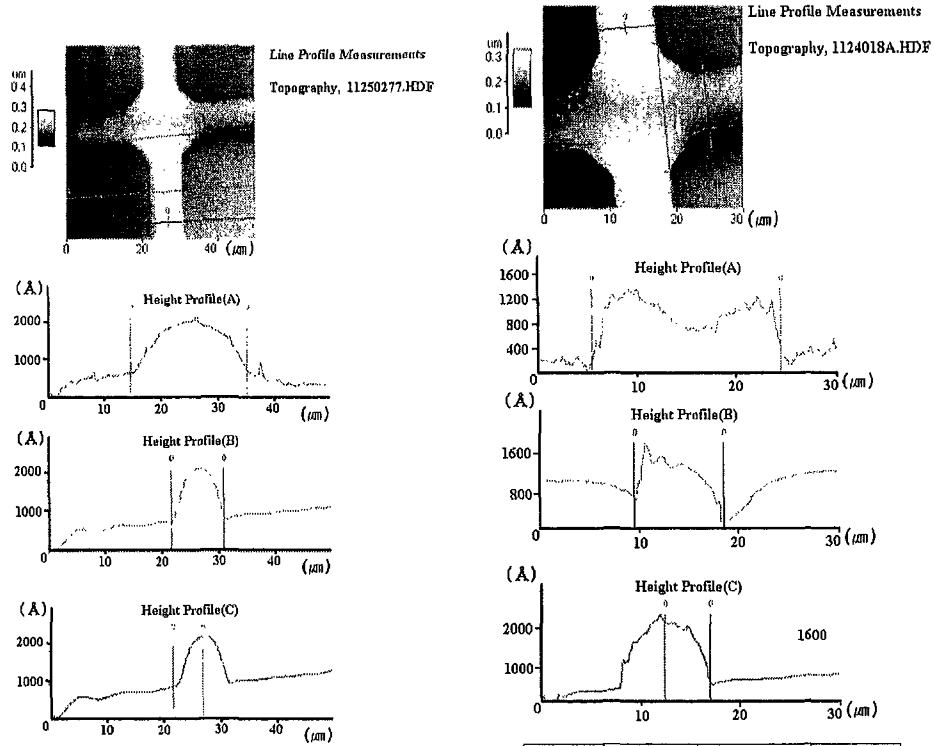

Line	Height(Å)	Distance(µm)	Angle(θ)
(A)(o-o)	80.3	20.7	0.00
(B)(o-o)	78.4	9.43	0.4
(C)(o-o)	1500	5.31	1.6

Line	Height(Å)	Distance(µm)	Angle(θ)
(A)(o-o)	119	19.2	0.00
(B)(o-o)	565	8.98	0.4
(C)(o-o)	1780	4.61	2.2

FIG. 3.F.6. AFM images and profile measurements of the imprinted APS patterns: (a) A=10, B=20, C=120, (b) A=10, B=20, C=160 (all numbers in µm).

The PDMS microstamps described in Sec. II are soaked in pure water for a day for washing, then dipped in a solution of APS just for a few seconds prior to stamping[8 9]. Nitrogen gas is used to remove the extraneous APS solution and dry the patterned surface of microstamp. Subsequently, the dried APS pattern is imprinted carefully on a clean microscope slide glass for 5 min. The imprinted APS grid patterns are then directly quantified by LFM and AFM. The LFM image and the AFM image respectively shown in Fig. 3.F.5 and Fig. 3.F.6, well illustrate the actual imprinted APS pattern. Both are taken with the CP-AFM (Park Scientific Instruments) with a combined AFM/LFM head. All measurements are carried out with a force constant 0.05 N/m and scanning mode of 100 µm at room temperature in a contact mode. A 256 x 256 pixel image is scanned at a rate of 1 frame/s. The set point is 1.5 nN.

The six different profiles shown in Fig. 3.F.6 clearly indicate that APS patterns are indeed imprinted successfully only on the designated area and none otherwise. Measurements on the nominal path width (A), intersection node diameter (B), and the inter-nodal distance (C) are quite consistent with the originally designed values. The layer thickness of the imprinted APS, however, varies gradually from 1200 Å to 2000 Å across the track. The fine control on the thickness of the coated APS is yet to be made.

Section 3.F.3) Results

After the APS micro-patterns are imprinted on a slide glass plate as described in Sec. III, a glass culture ring is attached with Sylgard for containing cells and culture solution. Once the culture ring is firmly attached to the glass slide, the cell culture process proceeds as illustrated in Fig. 3.F.7. For this preliminary study that we have used dissociated heart cells of neonatal mouse just for the ease of sample preparation. First, 200 $\mu\ell$ of dissociated heart cell suspension is poured into the prepared culture chamber and placed for approximately 1 hour to settle on the surface of the imprinted area. The final cell population density is roughly 7.0×10^3 cells/cm^2. Later, an additional 1.5 cc cell culture medium is added. The used culture medium is a mixture of DMEM + 10% FBS + Antibiotics (penicillin +

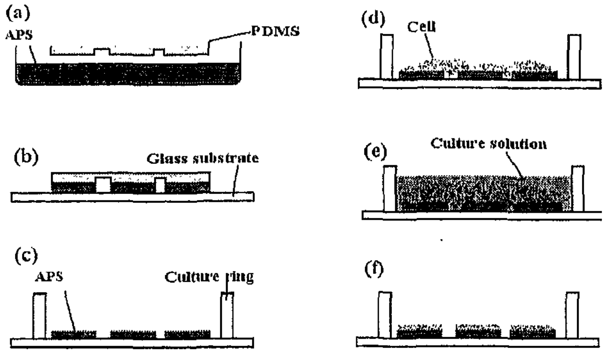

FIG. 3.F.7. Experimental procedure for patterned heart cell network culture: (a) PDMS dipped briefly in a solution of APS; (b) stamping APS to glass slide for 5 min; (c) culture ring attachment; (d) heart cell attachment; (e) cells in culture medium; and (f) final cell culture on the APS coated area.

---

[8][9] David A. Stenger and Thomas M. Mckenna, "Enabling Technologies for Cultured Neural Networks," Academic Press, (1999)

streptomycin). The culture chamber is then stored in a moisture and CO2 (95%) controlled incubator at 37 °C and monitored twice per day. Half of the old culture medium is replaced everyday. A similar experimental protocol can be used for neuronal cells as well.

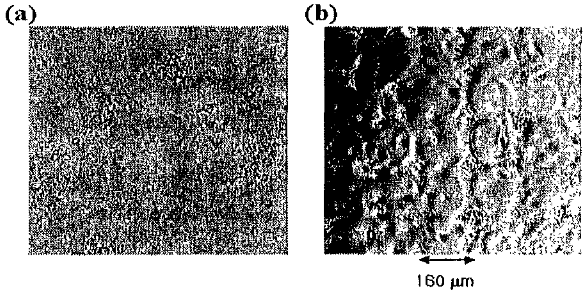

FIG. 3.F.8. Photographs of the heart cell culture: (a) with a square-grid pattern of APS only and (b) with the same square-grid pattern of APS and self-assembled OTE coating in non-patterned area. Both images are taken two weeks after plating at the initial density of 7.0×10^3 cells/cm^2. The square-grid cellular network shown in (b) can be maintained for more than a month in a controlled incubator. Note that the individual cells can not be identified in the square-grid network of (b), since they form a three dimensional mound in which cells are perfused together.

With the series of experimental procedures described above, however, our initial attempts for developing a patterned network of cells all have failed. The dissociated heart cells grow everywhere without any preference for a particular area for attachment, regardless of the imprinted APS pattern. This failure is believed to be originating from a little difference in the cytophilicity between APS patterned area and the bare background glass substrate[90]. Recently, we have resolved this problem by treating the glass plate with octadecyltriethoxysilane (OTE) afterthe APS imprinting job is processed.

The difference is quite dramatic as shown in Fig. 3.F.8. This time, cells have shown a strong preference to the APS covered grids, and practically there is no cell left in the untreated surface. At the beginning, individual heart cells are plated uniformly on the APS patterned culture plate. Then, approximately over a time duration of few days, cells migrate toward the APS covered grid area. By this time, the individual heart cells fuse into a thin cellular membrane through gap-junctions as they grow in sizes. The individual cells can not be easily distinguished in the bright-field optical image shown in Fig. 3.F.8, and only a smooth network of thin cellular membrane is evident. Such a cellular network is also obtained with other stamps differing in sizes, except for the smallest one with the inter-node-distance $C=80$ μm. Obviously, the cell density has been too high for this case. It is also noticed that the actual

---

[90] Private communication with Dr. Bruce Wheeler.

width of the cellular network grid thus formed is a few times wider than the patterned track width of APS.

Section 3.F.4) Discussion

Biological cell network by design is no longer a conceptual idea but has become feasible in laboratory experiments. Specifically, we have demonstrated that the imprinting of micro grid patterns of cytophilic chemical reagent APS followed by an uniform surface treatment of hydrophobic OTE is capable of producing a guided biological cell network. We believe this technical achievement is a very important step toward the understanding of how cells communicate each other. Although our preliminary experiments are conducted with heart cells only, the same technique can be also applied for building a simple neuronal network. A simplified neuronal network can be integrated to the multi-electrode array plate as well, so that one-to-one correspondence between a micro-electrode and one particular neuron of the relevant network becomes possible. In turn, the integrated system can be connected to a host of external electronics for both way communications. This will then become an ultimate system for probing the dynamic process of cell-to-cell signaling, synaptic plasticity associated with learning, and neuronal signal processing, just to name a few. The micro-stamping techniques combined with the advancement on multi-electrode array plate technology is to shed a light on the long-sought secrets behind neuro-spike signals.

Section 3.G Substance P in Photic resetting of circadian pacemakers in rat hypothalamus

Glutamate is considered to be the primary neurotransmitter in the retinohypothalamic tract (RHT), which delivers photic information from the retina to the suprachiasmatic nucleus (SCN), the locus of mammalian circadian pacemaker. However, substance P (SP) also has been suggested to play a role in retinohypothalamic transmission. In this study, we sought evidence that SP from the RHT contributes to photic resetting of the circadian pacemaker and further explored the possible interaction of SP with glutamate in this process. In rat hypothalamic slices cut parasagittally, electrical stimulation of the optic nerve in early and late subjective night produced a phase delay (2.4±0.5 hr; mean±SEM) and advance (2.6±0.3hr) of the circadian rhythm of SCN neuronal firing activity, respectively. The SP antagonist L-703,606 (10 μM) applied to the slices during the nerve stimulation completely blocked the phase shifts. Likewise, a cocktail of NMDA (2-amino-5-phosphonopentanoic acid, 50 μM) and non-NMDA (6,7-dinitroquinoxaline-2,3-dione, 10 μM) antagonists completely blocked the shifts. Exogenous application of SP (1 μM) or glutamate (100 μM) to the slices in early subjective night produced a phase delay (3*h*) of circadian firing activity rhythm of SCN neurons. Co-application of the NMDA and non-NMDA antagonist cocktail (as well as L-703,606) resulted in a complete blockade of the SP-induced phase delay. Whereas, L-703,606 (10 μM) had no effect on the glutamate-induced delay. These results suggest that SP, as well as glutamate, has a critical role in photic resetting. Further, the results suggest that the two agonists act in series, SP working upstream of glutamate.

Section 3.G.1) Motivation & Background

The retinohypothalamic tract RHT is a neural pathway arising from a subset of retinal ganglion cells and projecting to the (SCN)[91] [92] a hypothalamic region that contains the circadian pacemaker in mammals.[93] [94] Photic information conveyed to the SCN via the RHT is sufficient and essential for entrainment of the circadian pacemaker to the environmental light-dark cycle[95]. Previous studies have provided strong evidence that the excitatory amino acid (EAA) glutamate is a neurotransmitter employed by the RHT.[96]

However, accumulating data have suggested that SP also plays a neurotransmitter or neuromodulator role in retinohypothalamic transmission. SP-containing nerve fibers are concentrated in the ventral region (i.e., the retinorecipient portion) of the rat SCN,[97] [98] and retinal fibers make synaptic contacts with SP receptor-positive dendrites in the ventral part of the rat SCN.[99] SP applied

---

[91] Hendrickson AE, Wagoner N, Cowan WM (1972) An autoradiographic and electron microscopic study of retino-hypothalamic connections. Z Zellforsch Microsk Anat 135:1-26.

[92] Moore RY, Lenn NJ (1972) A retinohypothalamic projection in the rat. J Comp Neurol 146:1-14.

[93] Morin LP (1994) The circadian visual system. Brain Res Rev 67:102-127.

[94] Meijer JH, Rietveld WJ (1989) Neurophysiology of the suprachiasmatic circadian pacemaker in rodents. Physiol Rev 69:671-707.

[95] Rusak B, Boulos Z (1981) Pathways for photic entrainment of mammalian circadian rhythms. Photochem Photobiol 34:267-273.

[96] Ebling FJP (1996) The role of glutamate in the photic regulation of the suprachiasmatic nucleus. Prog Neurobiol 50:109-132.

[97] Takatsuji K, Miguel-Hidalgo J-J, Tohyama M (1991) Substance P-immunoreactive innervation from the retina to the suprachiasmatic nucleus in the rat. Brain Res 568:223-229.

[98] Mikkelsen JD, Larsen PJ (1993) Substance P in the suprachiasmatic nucleus of the rat: an immunohistochemical and in situ hybridization study. Histochemistry 100:3-16.

[99] Takatsuji K, Senba E, Mantyh PW, Tohyama M (1995) A relationship between substance P receptor and retinal fibers in the rat suprachiasmatic nucleus. Brain Res 698:53-61.

exogenously to rodent hypothalamic slices alters the unit activity of SCN neurons[100] [101] [102] and can cause phase shifts in the circadian rhythms of SCN neuronal activity (Shibata et al., 1992). Intracerebroventricular or systemic injection of a SP antagonist in the hamster blocks the expression of Fos-like protein in the SCN[103] and the phase advances of circadian locomotor activity rhythm[104] induced by light pulses. Moreover, SP antagonist applied to rat hypothalamic slices depresses excitatory postsynaptic currents (EPSCs) of SCN neurons evoked by optic nerve stimulation.[105]

On the other hand, there are also some results that throw doubt on the role for SP in retinohypothalamic transmission. Neurons expressing SP receptors in the rat SCN are mainly located in the dorsolateral margin of the nucleus, not the retinorecipient region,[106] and the effects of ocular enucleation on the density of SP-immunoreactive nerve fibers and terminals in the SCN are inconsistent; although a couple of laboratories have reported a significant reduction of SP immunoreactivity in the rat SCN, [98] [99] others have failed to detect a decrease in SP-immunoreactive elements in both the rat and hamster SCN.[107] [108] Thus, it still remains to be determined whether or not SP plays a RHT neurotransmitter or neuromodulator role.

In this study, using rat hypothalamic slices containing both the SCN and optic nerve, we sought physiological evidence that SP from RHT terminals contributes to photic resetting of the suprachiasmatic circadian pacemaker. In addition, we explored the possible interactions between SP and glutamate in photic resetting. In the first set of experiments, we examined the effects of SP and EAA antagonists on the phase shifts of circadian firing rhythms induced by optic nerve stimulation. In the second set, we examined the effects of SP and EAA antagonists on the phase-shifting effect of exogenously applied SP or glutamate.

---

[100] Shibata S, Tsuneyoshi A, Hamada T, Tominaga K, Watanabe S (1992) Effect of substance P on circadian rhythms of firing activity and the 2-deoxyglucose uptake in the rat suprachiasmatic nucleus in vitro. Brain Res 597:257-263.

[101] Shirakawa T, Moore RY (1994) Responses of rat suprachiasmatic nucleus neurons to substance P and glutamate in vitro. Brain Res 642:213-220.

[102] Piggins HD, Cutler DJ, Rusak B (1995) Ionophoretically applied substance P activates hamster suprachiasmatic nucleus neurons. Brain Res Bull 37:475-479.

[103] Abe H, Honma S, Shinohara K, Honma K-I (1996) Substance P receptor regulates the photic induction of Fos-like protein in the suprachiasmatic nucleus of Syrian hamsters. Brain Res 708:135-142.

[104] Challet E, Naylor E, Metzger JM, MacIntyre DE, Turek FW (1998) An NK_1 receptor antagonist affects the circadian regulation of locomotor activity in golden hamsters. Brain Res 800:32-39.

[105] Kim YI, Kim SH, Kim DY, Lee HW, Shin H-C, Chung J-M, Han HC, Na HS, Hong SK (1999) Electrophysiological evidence for the role of substance P in retinohypothalamic transmission in the rat. Neurosci Lett 274:99-102.

[106] Mick G, Maeno H, Kiyama H, Tohyama M (1994) Marginal topography of neurons expressing the substance P receptor in the rat suprachiasmatic nucleus. Brain Res Mol Brain Res 21:157-161.

[107] Otori Y, Tominaga K, Fukuhara C, Yang J, Yamazaki S, Cagampang FR, Okamura H, Inouye ST (1993) Substance P-like immunoreactivity in the suprachiasmatic nucleus of the rat. Brain Res 619:271-277.

[108] Hartwich M, Kalsbeek A, Pévet P, Nürnberger F (1994) Effects of illumination and enucleation on substance-P-immunoreactive structures in subcortical visual centers of golden hamster and Wister rat. Cell Tissue Res 277:351-361.

Section 3.G.2) Methods

Animals and housing Male Sprague-Dawley rats (n=72; 50-200g) purchased from Daehan Experimental Animal Co. (Eumsung, Korea) were used in this study. The experimental procedures described below were in accordance with the guidelines set by the Korea University College of Medicine Animal Research Policies Committee. Before electrophysiological experiments, the animals were housed in a temperature-controlled room (22-24°C) with a 12:12 h light/dark schedule for at least a week. Zeitgeber time (ZT) 0:00 h was defined as the time of lights-on and ZT 12:00 h as the time of lights-off in the colony.

Brain slice preparation The rats were anesthetized with sodium pentobarbitone (100 mg/kg, ip.) between ZT 10:30 h and 11:30 h, and the brain was quickly excised and submerged in ice-cold physiological saline (composition in mM: 124 NaCl, 1.3 $MgSO_4.7H_2O$, 3 KCl, 1.25 NaH_2PO_4, 26 $NaHCO_3$, 2.4 $CaCl_2$, 10 glucose) supplemented with gentamicin (50 mg/l). After about 1 min of chilling, the brain was trimmed to a block containing the hypothalamus and optic nerves. With the use of a vibroslicer (World Precision Instruments, Sarasota, FL), two parasagittal slices (400-500 μm thickness), each containing one optic nerve (4-7 mm) and an SCN, were cut from the tissue block. During the slicing, the tissue was maintained in ice-cold physiological saline. One of the slices was transferred to a modified Hass-type gas interface recording chamber (Haas et al., 1979) and superfused continuously, at a rate of 0.4 ml/min, with warm physiological saline (35°C, pH 7.4) aerated with 95% O_2/5% CO_2. Warm air (35°C) humidified by 95% O_2/5% CO_2 was also continuously blown over the slice to further ensure adequate oxygenation of the cells in the tissue.

Optic nerve stimulation and electrophysiological recording On the first day *in vitro*, the optic nerve was stimulated with a suction electrode; constant current pulses of 0.5-mA intensity (1.0-ms biphasic square wave, 5 Hz) or 0-mA intensity (in the case of sham stimulation) were applied for 15 min, starting at ZT 14:00 h (i.e., early subjective night) or 22:00 h (i.e., late subjective night). To make sure that the stimulation at 0.5-mA intensity did not activate SCN neurons directly by current spread, we performed some control experiments using the whole-cell current-clamp technique; the electrodes (tip diameter: about 2 μm ; resistances: about 3MΩ) were filled with a solution (pH 7.3) that was composed of (mM): 140 K-gluconate, 10 HEPES, 2 $MgCl_2$, 1 $CaCl_2$, 11 EGTA, 2 K_2ATP. In these experiments, the stimulation intensity was varied from 0.1 to 1.0 mA. In no case (10 cells tested in 3 slices) did the stimulation at 0.5-mA intensity elicit action potentials directly from SCN neurons, but it clearly evoked excitatory postsynaptic potentials with a constant latency (9-15 ms; in 5 of 10 cells tested in 3 slices) (Fig. 3.G.1).

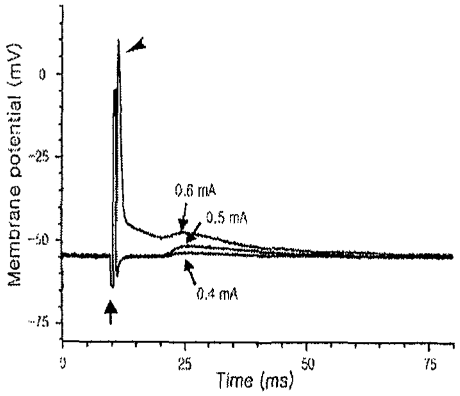

FIG. 3.G.1. Postsynaptic responses of an SCN neuron to three different intensities of optic nerve stimulation. At all of these intensities, the stimulation (upward arrow) evoked EPSPs with an 11 msec latency. At 0.6mA intensity, the stimulation also evoked an action potential (arrowhead) because of current spread to the site of recording; note the short latency of this action potential.

Extracellular single-unit recordings were made on the second day *in vitro*, using glass electrodes (4-5 MΩ) filled with 3-M NaCl (pH 7.4). Typically 8 units were sampled every hour (range: 5-15 units). The sampling was not restricted to any particular region of the SCN. The single-unit activities were recorded for 1 min for each cell and grouped into a 2-h running average with 1-h lag to determine the time-of-peak of circadian firing activity rhythm.[109] This time point was adopted as the phase reference point of the rhythm.

Drugs In the first set of experiments (see above), the SP antagonist L-703,606 (0.1-10 μM; selective for NK_1 receptors; RBI, Natick; MA) or a cocktail of the NMDA antagonist 2-amino-5-phosphonopentanoic acid (AP5, 50 μM; Sigma, St. Louis, MO) and the non-NMDA antagonist 6,7-dinitroquinoxaline-2,3-dione (DNQX, 10 μM; Sigma) was bath-applied for 30 min on the first day *in vitro*. This application started 10 min before sham or genuine optic nerve stimulation. In the second set of experiments, SP (1 μM; Sigma) or glutamate (100 μM; Sigma) was bath-applied for 30 min on the first day *in vitro*, starting at ZT 14:00 h. These agents were applied alone or together with L-703,606

---

[109] Ding JM, Chen D, Weber ET, Fairman LE, Rea MA, Gillette MU (1994) Resetting of the biological clock: mediation of nocturnal circadian shifts by glutamate and NO. Science 266:1713-1717.

(10 μM) or the NMDA and non-NMDA antagonist cocktail (50- μM AP5 plus 10- μM DNQX).

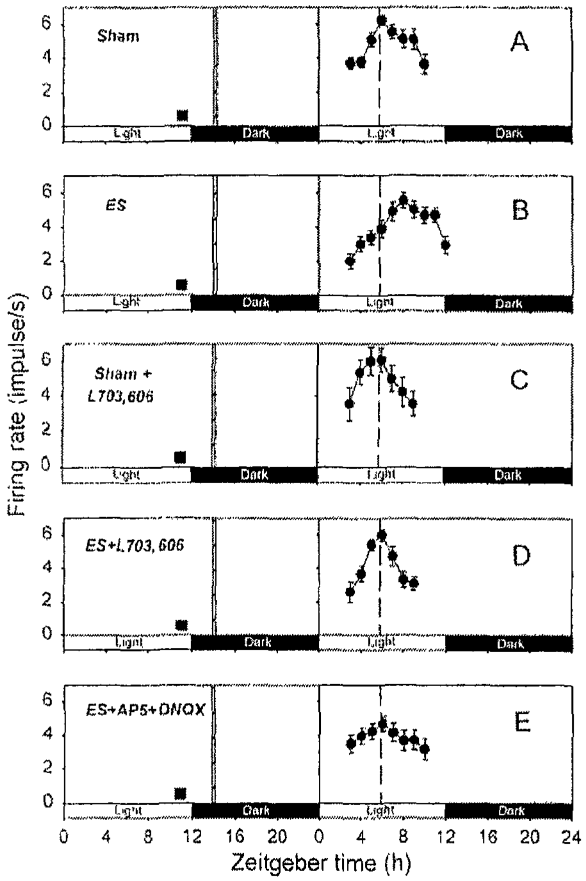

FIG. 3.G.2. Effects of SP and EAA antagonists on the phase delay of circadian firing rhythm induced by optic nerve stimulation at ZT 14 hr. The plots in *A-E* show representative data from single slices. In each graph, 2 hr running means (± SEM) of firing rates are plotted against ZT to determine the time of peak firing activity. The projected light and dark phases of the animal room are indicated with *open* and *filled horizontal bars*, respectively. Each of the experiments in *A-E* was repeated four to seven times (see text) for determination of the times of peak firing activities. These were compared across different experiments using ANOVA and Tukey tests.*A*, *Sham*, Sham stimulation. *B*, *ES*, Optic nerve stimulation. *C*, *Sham* + *L*703,606, *L*-703,606 application during sham optic *D*, *ES* + *L*703,606, *L*-703,606 application during optic nerve stimulation. E. ES + AP5 + DNQX, Application of the AP-5-DNQX cocktail during optic nerve stimulation. *Dashed vertical line*, Average time of peak firing activity for the slices subjected to sham optic nerve stimulation; filled square, time of slice preparation; *hashed vertical bar*, time of optic nerve stimulation.

Statistical analyses Numerical data are expressed in mean ± SEM. An ANOVA was used to check the presence of significant variance among data from different experimental groups, and Tukey test was performed to see whether there was any significant difference between data from two different experimental groups. $P<0.05$ was considered to be significant.

Section 3.G.3) Results

Effects of SP and EAA antagonists on the phase delays produced by optic nerve stimulation in the early subjective night (ZT 14) In control slices subjected to sham stimulation of the optic nerve, the peaks of circadian firing activity rhythms were detected at ZT 4-7 h (ZT 5.8 ± 0.5 h, n=5; Fig. 3.G.2A). In optic nerve-stimulated slices, however, the peaks of circadian rhythms were at ZT 7-10 h

(ZT 8.2 ± 0.5 h, n=6; Fig. 3.G.2B), indicating that optic nerve stimulation produced phase delays of the rhythms. The mean delay was 2.4 ± 0.5 h (n=6), which was statistically significant (Fig. 3.G.4A).

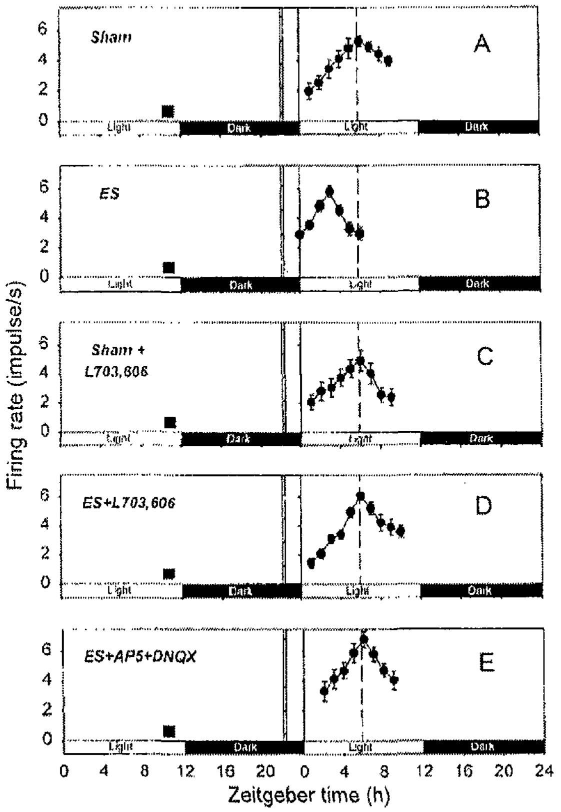

FIG. 3.G.3. Effects of SP and EAA antagonists on the phase advance of circadian firing rhythm induced by optic nerve stimulatin at ZT 22 hr. Each of the experiments in *A-E* was repeated four to six times (see text). The format of this figure is the same as that of Figure 3.G.2.

In slices treated with L-703,606 (10 μM) during sham optic nerve stimulation, the peaks of circadian firing activity rhythms were at ZT 5-6 h (ZT 5.8 ± 0.3 h, n=4; Fig. 3.G.2C), similar to those of control slices. This indicated that L-703,606 by itself had no phase-shifting effect. Nevertheless, L-703,606 (10 μM) treatment completely blocked the optic nerve stimulation-induced phase delay (Fig. 3.G.2D); the times-of-peaks of circadian rhythms in slices subjected to both optic nerve stimulation and L-703,606 treatment were in the range of ZT 5-6 h (ZT 5.4 ± 0.2 h, n=7). These peak times were significantly different from those of optic nerve-stimulated, but not control, slices. The effects of 0.1-, 1- and 10-μM L-703,606 on the optic nerve stimulation-induced phase delay are summarized in Fig. 3.G.4A. Statistically significant blockade of the phase shift was obtained only at 10 μM, although a partial blockade was noticed at 1 μM.

Treatment of slices with a cocktail of EAA antagonists AP5 (50 μM) and DNQX (10 μM) was also effective in preventing the optic nerve stimulation-induced phase delay (Fig. 3.G.2E and 4A). In EAA antagonist-treated slices, the times-of-peaks of circadian rhythms were in the range of ZT 5-7 h (ZT 6.0 ± 0.3 h, n=5; Fig. 3.G.2E). Again, these times-of-peaks were statistically different from those of optic nerve-stimulated, but not control, slices (Fig. 3.G.4A).

Effects of SP and EAA antagonists on the phase advances produced by optic nerve stimulation in the late subjective night (ZT 22) In control slices subjected to sham optic nerve stimulation, the peaks of circadian firing activity rhythms were at ZT 5-6 h (ZT 5.8 ± 0.2 h, n=6; Fig. 3.G.3A). In contrast, in optic nerve-stimulated slices, the peaks were detected at ZT 2-4 h (ZT 3.2 ± 0.3 h, n=6; Fig. 3.G.3B), indicating phase advances of the rhythms. These phase shifts (2.6 ± 0.3 h, n=6) were statistically significant (Fig. 3.G.4B).

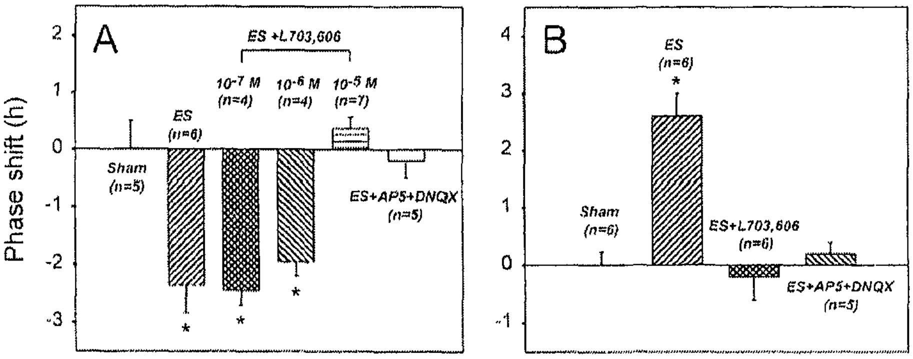

FIG. 3.G.4. Summary of the effects of SP and EAA antagonists on the optic nerve stimulation-induced phase delay (*A*) and advance (*B*). The ANOVA test indicated a significant variance among the data from different experiments ($p<0.001$) in both *A* and *B*. The Tukey test further indicated that the asterisk-labeled data were significantly different from the remainder. However, this test indicated that there was no significant difference among the asterisk-labeled data in *A* and among the remaining data in *A* and *B*.

L-703,606 application (10 μM) during sham stimulation of the optic nerve had no significant effect on the phases of circadian rhythms; their peaks were detected at ZT 5-6 (ZT 5.5 ± 0.3 h, n=4; Fig. 3.G.3C). On the other hand, L-703,606 (10 μM) treatment completely blocked the phase advance produced by optic nerve stimulation (Fig. 3.G.3D and 3.G.4B); the times-of-peaks of circadian rhythms in slices subjected to both optic nerve stimulation and L-703,606 treatment were in the range of ZT 5-7 h (ZT 6.0 ± 0.4 h, n=6). These peak times were significantly different from those of optic nerve-stimulated, but not control, slices.

The cocktail of the EAA antagonists was also effective in blocking the optic nerve stimulation-induced phase advance (Fig. 3.G.3E and 3.G.4B). The times-of-peaks of circadian rhythms in EAA antagonist-treated slices were in the range of ZT 5-6 h (ZT 5.6 ± 0.2 h, n=5), which were not statistically different from those of control slices.

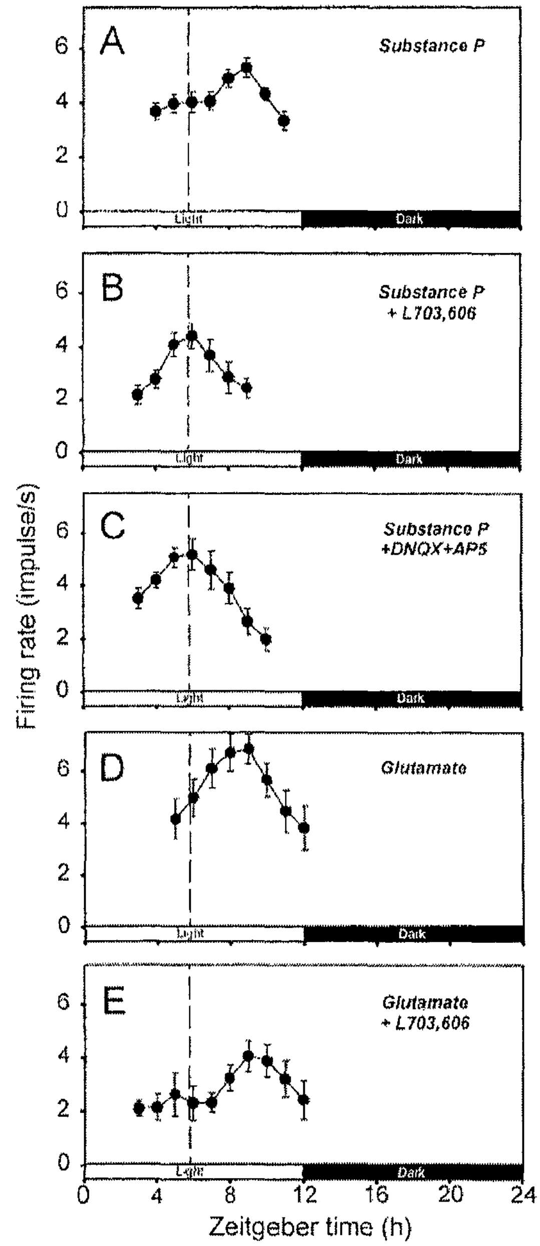

FIG. 3.G.5. Effects of SP and EAA antagonists on the phase delay induced by exogenous SP or glutamate application. The plots in A-E show representative data from single slices. In each graph. 2 hr running means (± SEM) of firing rates are plotted against ZT. The *dashed vertical line* in each plot indicates the average time of peaks of circadian rhythms observed in control slices (i.e., those subjected to sham optic nerve stimulation). The mean times of peaks determined for the experimental conditions in *A-E* were ZT 8.8 ± 0.4 hr (*n*=6), 5.5 ± 0.5 hr (*n*=4)*, 5.8 ± 0.2 hr (*n*=5)*, 9.0 ± 0.0 hr (*n*=4), and 9.0 ± 0.4 hr (*n*=4), respectively. The ANOVA test indicated a significant variance among these values (p <0.001). The mean values denoted with asterisks in the above list were significantly different from the remainder, but they were not different from each other (Tukey test). The values not labeled with asterisks were not significantly different from one another (Tukey test).

Effects of SP and EAA antagonists on the phase delay induced by exogenous SP or glutamate application Bath application of SP (1 μM) and glutamate (100 μM) in early subjective night produced an average of 3.0-h and 3.2-h phase delay of circadian firing activity rhythm, respectively (Fig. 3.G.5A and D). Co-application of L-703,606 (10 μM) or the NMDA and non-NMDA antagonist cocktail (50-μM AP5 plus 10-μM DNQX) resulted in a complete blockade of the SP-induced phase shift (Fig. 3.G.5B and C). However, L-703,606 had no significant effect on the glutamate-induced delay (Fig. 3.G.5E).

Section 3.G.4) Discussion

Role of SP in photic resetting and its interaction with glutamate

The present study demonstrated that not only the cocktail of NMDA and non-NMDA antagonists, but also the selective SP antagonist L-703,606 completely blocked the phase shifts of circadian firing activity rhythm in the SCN induced by optic nerve stimulation. These results strongly suggest that SP, as well as glutamate, released from RHT terminals plays a critical role in photic resetting of the circadian pacemaker. Furthermore, the results suggest that SP and glutamate interact. Previous studies showed that SP potentiated the excitatory responses of SCN neurons to glutamate and NMDA.[101] [102] Also, our unpublished data from parasagittal hypothalamic slices indicate that SP potentiates NMDA-induced currents in retinorecipient SCN neurons. Thus, the interaction between SP and glutamate may occur postsynaptically, but it may also occur presynaptically. The finding of [110] that SP causes glutamate and aspartate release from hamster SCN slices is consistent with this idea.

SP does not play a permissive role for glutamate and vice versa because glutamate or SP alone was sufficient to produce a phase shift of circadian rhythm.[100] [111] The present study suggest that if the two agonists interact, they act in series with SP working upstream of glutamate, since the SP antagonist L-703,606 had no effect on the glutamate-induced phase shift whereas the EAA antagonist cocktail completely blocked the SP-induced shift. Data from [110] showing that the NMDA antagonist MK-801 reduces the SP-induced phase delay of the circadian firing rhythm also provide support for this hypothesis.

The present results suggesting a critical role for SP in photic resetting were somewhat

---

[110] Hamada T, Yamanouchi S, Watanabe A, Shibata S, Watanabe S (1999) Involvement of glutamate release in substance P-induced phase delays of suprachiasmatic neuron activity rhythm in vitro. Brain Res 836:190-193.

[111] Ding JM, Chen D, Weber ET, Fairman LE, Rea MA, Gillette MU (1994) Resetting of the biological clock: mediation of nocturnal circadian shifts by glutamate and NO. Science 266:1713-1717.

surprising because retinohypothalamic transmission was not dependent on SP.[105] This study demonstrated that a SP antagonist only slightly depressed the EPSCs of SCN neurons evoked by optic nerve stimulation. However, it is possible that the role of SP was underestimated in this study, since the frequency of optic nerve stimulation was very low (0.033 Hz). In the present study, the stimulation frequency was 5 Hz. At this frequency, the SP release from optic nerve terminals might be large enough to explain the critical role of SP.

Our observation that the SP antagonist L-703,606 could block both the phase advances and delays of circadian rhythms is not in full agreement with the report of.[104] These investigators found that an intraperitoneal injection of another selective NK_1 receptor antagonist in the hamster blocked the light pulse-induced phase advances, not delays, of circadian locomotor activity rhythm. The disparity between our and Challet et al.'s results might be related to the difference in species; in the rat SCN, SP-containing nerve fibers and terminals are distributed throughout the nucleus, with the largest accumulation in its ventral part,[97] [98] whereas in the hamster SCN, SP-positive fibers are rare although a small cluster of SP neurons are located in the lateral aspect of the nucleus.[112] [113] [114] Thus, in the case of hamster, any SP released from nerve terminals might be derived from intrinsic SCN neurons, rather than from the RHT, and any action of a SP antagonist may be via receptors that never receive input from the RHT.

The disparity between our and Challet et al.'s findings might also be related to the difference in the site of drug action (SCN *vs.* whole brain) or experimental parameters examined (SCN neuronal firing *vs.* locomotor activity). However, it is unlikely to be due to non-specific actions of the SP antagonist used in the present study, since 1) L-703,606 had no phase-shifting effects by itself, 2) its effects were concentration-dependent and 3) it produced a selective blockade of the SP-induced (not glutamate-induced) phase delays.

Experimental paradigm

Recently it was reported that the circadian rhythm of SCN neuronal firing activity, recorded as a

---

[112] Morin LP, Blanchard J, Moore RY (1992) Intergeniculate leaflet and suprachiasmatic nucleus organization and connections in the golden hamster. Vis Neurosci 8:219-230.

[113] Swann JM, Macchione N (1992) Photoperiodic regulation of substance P immunoreactivity in the mating behavior pathway of the male golden hamster. Brain Res 590:29-38.

[114] Reuss S, Burger K (1994) Substance P-like immunoreactivity in the hypothalamic suprachiasmatic nucleus of Phodopus sungorus--relation to daytime, photoperiod, sex and age. Brain Res 638:189-195.

single daytime peak in coronal slices of the hamster brain, exhibited two distinct peaks when slices were cut in the horizontal plane.[115] In our parasagittal slices of the rat brain, however, dual daytime peaks have never been detected. Even in horizontal slices of the rat SCN, only a single peak was detected (personal communication, Dr. Burgoon, P. W., University of Illinois). Thus, the plane of section is unlikely to be a problem in studying the photic resetting mechanism.

A potential problem associated with the use of parasagittal slices is the washout of neurotransmitters and neuromodulators in the hours between slice preparation and optic nerve stimulation. However, we had shown that sizable EPSCs, which were sensitive to SP and EAA antagonists, could be evoked in SCN neurons by optic nerve stimulation for up to 12 hours after slice preparation.[105] Thus, the washout, if any, seems to be a minor problem.

A large number of studies used coronal hypothalamic slices to investigate the postsynaptic mechanisms of photic resetting. In these studies, bath application of a candidate neurotransmitter or neuromodulator of the RHT often substituted for photic stimulation, but direct RHT stimulation was seldom tried,[116] presumably due to the difficulty of specific RHT stimulation. In the present study, employing parasagittal slices, we showed that specific optic nerve (i.e., RHT) stimulation produced a phase advance or delay of the circadian rhythm of SCN neuronal activity with a phase response relationship very similar to that produced by light *in vivo*. Also, we demonstrated that the phase shifts were sensitive to SP and EAA antagonists. These results suggest that parasagittal hypothalamic slices are a viable *in vitro* model that allows investigation of both pre- and postsynaptic mechanisms of photic resetting.

---

[115] Jagota A, de la Iglesia HO, Schwartz WJ (2000) Morning and evening circadian oscillations in the suprachiasmatic nucleus in vitro. Nat Neurosci 3:372-376.

[116] Shibata S, Moore RY (1993) Neuropeptide Y and optic chiasm stimulation affect suprachiasmatic nucleus circadian function in vitro. Brain Res 615:95-100.

Chapter 4 Conclusion

The long-term goal of this research project is to build a bridge between nonlinear dynamics and neuroscience, setting a foundation for the new interdisciplinary field *neurodynamics*. The primary research objectives are, (1) to investigate diverse, yet, generic features of spatiotemporal patterns or self-organizations in coupled systems of nonlinear oscillators; (2) to develop simple and well-defined *in vitro* neuronal systems for the quantification of spatiotemporal activities of living biological neural networks; and (3) to understand spiking activities of the simplified network based on nonlinear time series analyses and the theory of pattern formation. During the first three years, our research emphasis is put on the first objective.

We revealed several new important phenomena of nonequilibrium pattern formation and successfully developed a proto-type living neural network as a well-defined model system for quantitative study. The most significant results are (1) the first experimental realization of complex periodic spiral waves and associated *line-defects*; (2) the first experimental demonstration of *spatial period-doublings* of basic lattice patterns by resonant mode interactions; (3) the experimental proof that *Substance P* plays a major role in photic resetting of suprachiasmatic nuclus (SCN); and (4) the successful development of a proto-type *neurochip* interfacing biological neural networks with micro-fabricated multi-electrode array (MEA) plate and designed networks of biological cells .

Chapter 5 Major Contribution

During the past two and half years, we have carried out world-class scientific researches and published several papers in premier research journals **(four in *Phys. Rev. Lett.* and one in *J. of Neuroscience*)** among others. In addition, three papers are currently being reviewed by *Phys. Rev. Lett.* Considering the fact that the total number of papers published in *Phys. Rev. Lett.* by Korean institutions and research centers all together is about 20-30 annually, our scientific achievement as a small research group is quite substantial. Indeed, we are one of the leading groups in the related field, being highly competitive in the international community. **We have definitely achieved more than our goal set out originally.**

References

1] M. Cross and P.C. Hohenberg, Rev. Mod. Phys. **65**, 851 (1993).

[2] L. Goryachev and R. Kapral, Phys. Rev. Lett. **76**, 1619 (1996).

[3] L. Goryachev, H. Chaté, R. Kapral, Phys. Rev. Lett. **80**, 873 (1998).

[4] L. Goryachev, H. Chaté, R. Kapral, Phys. Rev. Lett. **83**, 1878 (1999).

[5] R. Gallagher *et al.*, Science **284**, 79 (1999), Special section on complex systems.

[6] D. Walgraef, *Spatio-Temporal Pattern Formation* (Springer, New York, 1997).

[7] *Waves and Patterns in Chemical and Biological Media* H. L. Swinney and V. I. Krinsky (MIT/North-Holland, 1992).

[8] *Chemical Waves and Patterns*, edited by R. Kapral and K. Showalter (Kluwer, Dordrecht, 1995).

[9] L. Rensing, *Oscillations and Morphogenesis* (Marcel Dekker, New York, 1993).

[10] L. Glass, Physics Today **45**, No 8, 40 (1996).

[11] C. M. Hempel, P. Vincent, S. R. Adams, R. Y. Tsien, and A. I. Selverston, Nature **384**, 166 (1996).

[12] E. Ranta and V. Kaitala, Nature **390**, 456 (1997).

[13] B. Blasius, A. Huppert and L. Stone, Nature **399**, 354 (1999).

[14] R. H. Simoyi, A. Wolf, H. L. Swinney, Phys. Rev. Lett. **49**, 245 (1982).

[15] K. S. Scott, *Chemical Chaos* (Clarendon Press, Oxford, 1991).

[16] A. T. Winfree and S. H. Strogatz, Nature **311**, 611 (1984).

[17] A. S. Mikhailov, *Foundation of Synergetics I. Distributed Active Systems* (Springer-Verlag, Berlin, 1994).

[18] A. T. Winfree, *When time breaks down* (Princeton University Press, Princeton, 1987).

[19] G. Ertl, Science **254**, 1750 (1991).

[20] K. B. Migler and R. B. Meyer, Phys. Rev. E **48**, 1218 (1993).

[21] K. J. Lee, E. C. Cox, and R. E. Goldstein, Phys. Rev. Lett. **76**, 1174 (1996) and Pálsson, K. J. Lee, R. E. Goldstein, J. Franke, R. H. Kessin, and E. C. Cox, Proc. Natl. Acad. Sci. USA **94**, 13719 (1997) and references therein.

[22] A. S. Mikhailov, *Foundation of Synergetics I. Distributed Active Systems* (Springer-Verlag, Berlin, 1994) and references therein.

[23] J. Lechleiter, S. Girard, D. Clapham, and E. Peralta, Nature **350**, 505 (1991); L. Rensing, *Oscillations and Morphogenesis* (Marcel Dekker, New York, 1993).

[24] A. Goryachev, H. Chaté, R. Kapral, Phys. Rev. Lett. **83**, 1878 (1999) and references therein.

[25] J. -S. Park and K. J. Lee, Phys. Rev. Lett. **83**, 5393 (1999).

[26] None of the earlier studies reported such a case. The line-defects of P-2 spiral waves discussed in just decays quadratically in a continuous fashion.

[27] M. G. Rosenblum, A. S. Pikovsky, and J. Kurths, Phys. Rev. Lett. **76**, 1084 (1996); U. Parlitz, L. Junge, W. Lauterborn, and L. Kocarev, Phys. Rev. E **54**, 2115 (1996); K. J. Lee, Y. Kwak. and T. K. Lim, Phys. Rev. Lett. **81**, 321 (1998).

[28] D. Barkley, Phys. Rev. Lett. **72**, 164 (1994); G. Li, Q. Ouyang, V. Petrov, and H. L. Swinney, Phys. Rev. Lett. 77, 2105 (1996); L. Q. Zou, and Q. Ouyang, Phys. Rev. Lett. **85**, 1650 (2000); and S. -M. Hwang, W. G. Choe, and K. J. Leė, Phys. Rev. E **62**, 4799 (2000).

[29] Possible existence of epicycloid orbit -- the primary circle orbits the secondary circle in the opposite sense of its self-spinning – is also looked for in our system, in particular in a lower $[H^+]$ regime, but failed. The compound orbit starts significantly being influenced by the system boundary as the pitch of the relevant P-2 spiral becomes comparable to the size of our experimental system. Besides, the

image contrast becomes dramatically poor in the lower $[H^+]$ regime.

[30] S. Jakubith, H. H. Rotermund, W. Engel, A. von Oertzen, and G. Ertl, Phys. Rev. Lett. **65**, 3013 (1990).

[31] E. Bodenschatz, J. de Bruyn, G. Ahlers, and D. S. Cannell, Phys. Rev. Lett. **67**, 3078 (1991).

[32] K. B. Migler and R. B. Meyer, Phys. Rev. Lett. **66**, 1485 (1991); K. B. Migler and R. B. Meyer, Physica D **71**, 412 (1994).

[33] P. Umbanhowar, F. Melo, and H. L. Swinney, Physica A **1**, 1, (1997).

[34] A. T. Winfree, Science **181**, 937 (1973).

[35] A. N. Zaikin and A. M. Zhabotinsky, Nature **225**, 535 (1970).

[36] K. J. Lee, E. C. Cox, and R. E. Goldstein, Phys. Rev. Lett. **76**, 1174 (1996).

[37] A. T. Winfree, Chaos **1**, 303 (1991).

[38] D. Barkley, Phys. Rev. Lett. **72**, 164 (1994).

[39] G. Li, Q. Ouyang, V. Petrov, and H. L. Swinney, Phys. Rev. Lett. **77**, 2105 (1996), and the references therein.

[40] K. J. Lee, E. C. Cox, and R. E. Goldstein, Phys. Rev. Lett. **76**, 1174 (1996).

[41] K. J. Lee, Phys. Rev. Lett. **79**, 2907 (1997).

[42] D. P. Zipes and J. Jalife, *Cardiac Electrophysiology: From Cell to Bedside* (W. B. Saunders, Philadelphia, 1995).

[43] W. Rappel, F. Fenton, and A. Karma, Phys. Rev. Lett. **83**, 456 (1999).

[44] O. Steinbock, V. Zykov, and S. C. Müller, Nature **366**, 322 (1993).

[45] A. P. Muñuzuri, M. Gómez-Gesteira, V. Pérez-Muñuzuri, V. I. Krinsky, and V. Pérez-villar, Phys. Rev. E **50**, 4258 (1994).

[46] V. Petrov, Q. Ouyang, and H. L. Swinney, Nature **388**, 655 (1997); A. Lin *et al.*, ``Resonant Pattern Formation in a Spatially Extended Chemical System", in *Pattern Formation in Continuous and Coupled Systems* (Springer, New York, 1999), eds. M. Golubitsky, D. Luss, S. H. Strogatz.

[47] D. M. Goldschmidt, V. S. Zykov, and S. C. Müller, Phys. Rev. Lett. **80**, 5220 (1998).

[48] W. Rappel, F. Fenton, and A. Karma, Phys. Rev. Lett. **83**, 456 (1999).

[49] D. Barkley, M. Kness, L. S. Tuckerman, Phys. Rev. A **42**, 2489 (1990).

[50] Explicit Euler method is used for a 200×200 square-grid with no-flux boundary condition. The diffusion terms are evaluated by finite difference 9-point formula after computing the reaction terms. The grid size and the temporal step size are $\Delta x=0.16$ and $\Delta t=0.005$, respectively. Throughout this Letter, the distences are given in units of Δx and the time is given in units of $200\,\Delta t$.

[51] We focus on the dynamics and bifurcations of a spiral tip by varying A for a few different fixed values of f_m that are close to but smaller than the natural frequency of the unmodulated spiral. When $f_m > f_0$, the spiral tip is gradually repelled away from the modulation site, as discussed.

[52] The primary circle is actually a slightly squished circle (i.e., an ellipse) as discussed in [49].

[53] See, e.g., M. Cross and P. Hohenberg, Rev. Mod. Phys. **65**, 851 (1993).

[54] W. S. Edwards and S. Fauve, J. Fluid Mech. **278**, 123 (1994); Phys. Rev. E **47**, R788 (1993).

[55] A. Kudrolli, B. Pier, and J. P. Gollub, Physica D **123**, 99 (1998).

[56] H. Arbell and J. Fineberg, Phys. Rev. Lett. **81**, 4384 (1998).

[57] C. Wagner, H. W. Müller, and K. Knorr, Phys. Rev. Lett. **83**, 308 (1999).

[58] C. Wagner, H. W. Müller, and K. Knorr, ``Crossover from a square to a hexagonal pattern in Faraday surface waves", patt-sol/9911001 (1999).

[59] J. -C. Bacri, U. d'Ortona, and D. Salin, Phys. Rev. Lett. **67**, 50 (1991).

[60] T. Mahr and I. Rehberg, Europhys. Lett. **43**, 23 (1998).

[61] H. Müller, H. Wittmer, C. Wagner, J. Albers, K. Knorr, Phys. Rev. Lett. **78**, 2357 (1997).

[62] R. Rosenweig, *Ferrohydrodynamics*, Cambridge University Press, Cambridge (1985).

[63] D. Raitt and H. Riecke, Phys. Rev. E **55**, 5448 (1997).

[64] T. Mahr and I. Rehberg, Phys. Rev. Lett. **81**, 89 (1998).

[65] M. Silber and M. R. E. Proctor, Phys. Rev. Lett. **81**, 2450 (1998); M. Silber and A. C. Skeldon, Phys. Rev. E **59**, 5446 (1999).

[66] Experimental evidence of stable rhombic pattern was discussed earlier in a chemical reaction-diffusion system by Q. Ouyang *et. al.* [Chaos **3**, 707 (1993)]. However, their observation is markedly different from ours: their rhombic lattice has a broad spectrum of angles with a mean value of 60^0, whereas our rhombic lattice is essentially tiled by a single rhombus with an oblique angle far different from 60^0.

[67] Amplitude equations for a non-monotonic dispersion relation are constructed in two dimensional space, then investigated numerically with a pseudo-spectral method. We find stable rhombic pattern as well as stable square pattern. More details on this study will be published elsewhere.

[68] R. Lifshitz and D. M. Petrich, Phys. Rev. Lett. **79**, 1261 (1997).

[69] N. Tufillaro, R. Ramshankar and J. Gollub, Phys. Rev. Lett. **62**, 422 (1989).

[70] A. Kudrolli and J. P. Gollub, Physica D **97**, 133 (1996).

[71] A. Goryachev and R. Kapral, Phys. Rev. Lett. **76**, 1619 (1996).

[72] A. Goryachev, H. Chaté and R. Kapral, Phys. Rev. Lett. **80**, 873 (1998).

[73] A. Goryachev, H. Chaté and R. Kapral, Phys. Rev. Lett. **83**, 1878 (1999).

[74] J.-S. Park and K. J. Lee, Phys. Rev. Lett. **83**, 5393 (1999).

[75] H. Arbell and J. Fineberg, Phys. Rev. Lett. **84**, 654 (2000).

[76] H. Arbell and J. Fineberg, Phys. Rev. Lett. **85**, 756 (2000).

[77] T. Mahr and I. Rehberg, Europhys. Lett. **43**, 23 (1998).

[78] H.-J. Pi, S.-y. Park, J. Lee, and K. J. Lee, Phys. Rev. Lett. **84**, 5316 (2000).

[79] The physical properties of EMG901 (EMG909) are, density ρ =1.53 (1.02) gm/ml, surface tension σ =27.5 (27.5) g/s^2, initial magnetic susceptibility χ =3.00 (0.80), magneti saturation M_s=600 (200) gauss, dynamic viscosity η=10 (6) cp, yielding a critical field of static Rosensweig instability 90.5 (168.2) gauss, respectively.

[80] Since the acquired full image is not sufficiently large to reveal the subharmonic Fourier peaks clearly, we quantified this transition by directly measuring the ratio (*m*) of two different cell sizes along the *x*-axis. The order parameter *m* decays continuously from $2S_l$ to $2S_a$. The driving frequency f is varied while maintaining ΔH =0.30 H_C.

[81] Our 1R pattern has the same origin of the ``two-mode rhomboid" ($2kR$) pattern described in[75] xcept that all four Fourier modes of 1R pattern are resonant modes whereas only two out of four are such for the $2kR$ pattern.

[82] The bistable ranges are typically an order of δf = 0.1Hz and $\delta\left[\frac{\Delta H}{H_c}\right]$= 0.02.

[83] Macro Bove, Massimo Grattarola, Sergio Martinoia and Giovanni Verreschi "Interfacing cultured neurons to planar substrate microelectrodes: characterization of the neuron-to-microelectrode junction," Bio-electrochemistry and Bio-energetics 38, pp. 255-265 (1995)

[84] L. J. Breckenridge, R. J. A. Connolly and C. D. W. Wilkinson, "Advantages of using microfabricated extracellular electrodes for in vitro neuronal recording," J. Neurosci. Res., Vol. 42, pp. 266-276 (1995.)

[85] D. W. Branch, B. C. Wheeler, G. J. Brewer and D.E. Leckband, "Long-Term Maintenance of Patterns of Hippocampal Pyramidal Cells on Substrates of Polyethylene Glycol and Microstamped Polylysine," IEEE Trans. Biomedical Engineering, Vol. 47, No. 3, March (2000)

[86] J. M. Corey, A. L. Brunette, M. S. Chen, J. A. Weyhenmeyer, G., J. Brewer and B. C. Wheeler, "Differentiated B104 neuroblastoma cells are a high-resolution assay for micropatterned substrate," Journal of Neuroscience Methods, Vol. 75, pp. 91-97 (1997)

[87] N. S. Seong, S. M. Hwang, K. J. Lee, D. J. Ahn and J. Pak, "Fabrication and experiment of microstamp for neuron patterning," the 8th Korean Conference on Semiconductors, pp. 665-666 (2001)

[88] Amit Kumar and Georage M. Whitesides, "Patterned Condensation Figures as Optical Diffraction Gratings," Science, vol. 263, pp. 60-62, January (1994).

[89] David A. Stenger and Thomas M. Mckenna, "Enabling Technologies for Cultured Neural Networks," Academic Press, (1999)

[90] Private communication with Dr. Bruce Wheeler.

[91] Hendrickson AE, Wagoner N, Cowan WM (1972) An autoradiographic and electron microscopic study of retino-hypothalamic connections. Z Zellforsch Microsk Anat 135:1-26.

[92] Moore RY, Lenn NJ (1972) A retinohypothalamic projection in the rat. J Comp Neurol 146:1-14.

[93] Morin LP (1994) The circadian visual system. Brain Res Rev 67:102-127.

[94] Meijer JH, Rietveld WJ (1989) Neurophysiology of the suprachiasmatic circadian pacemaker in rodents. Physiol Rev 69:671-707.

[95] Rusak B, Boulos Z (1981) Pathways for photic entrainment of mammalian circadian rhythms. Photochem Photobiol 34:267-273.

[96] Ebling FJP (1996) The role of glutamate in the photic regulation of the suprachiasmatic nucleus. Prog Neurobiol 50:109-132.

[97] Takatsuji K, Miguel-Hidalgo J-J, Tohyama M (1991) Substance P-immunoreactive innervation from the retina to the suprachiasmatic nucleus in the rat. Brain Res 568:223-229.

[98] Mikkelsen JD, Larsen PJ (1993) Substance P in the suprachiasmatic nucleus of the rat: an immunohistochemical and in situ hybridization study. Histochemistry 100:3-16.

[99] Takatsuji K, Senba E, Mantyh PW, Tohyama M (1995) A relationship between substance P receptor and retinal fibers in the rat suprachiasmatic nucleus. Brain Res 698:53-61.

[100] Shibata S, Tsuneyoshi A, Hamada T, Tominaga K, Watanabe S (1992) Effect of substance P on circadian rhythms of firing activity and the 2-deoxyglucose uptake in the rat suprachiasmatic nucleus in vitro. Brain Res 597:257-263.

[101] Shirakawa T, Moore RY (1994) Responses of rat suprachiasmatic nucleus neurons to substance P and glutamate in vitro. Brain Res 642:213-220.

[102] Piggins HD, Cutler DJ, Rusak B (1995) Ionophoretically applied substance P activates hamster suprachiasmatic nucleus neurons. Brain Res Bull 37:475-479.

[103] Abe H, Honma S, Shinohara K, Honma K-I (1996) Substance P receptor regulates the photic induction of Fos-like protein in the suprachiasmatic nucleus of Syrian hamsters. Brain Res 708:135-142.

[104] Challet E, Naylor E, Metzger JM, MacIntyre DE, Turek FW (1998) An NK_1 receptor antagonist affects the circadian regulation of locomotor activity in golden hamsters. Brain Res 800:32-39.

[105] Kim YI, Kim SH, Kim DY, Lee HW, Shin H-C, Chung J-M, Han HC, Na HS, Hong SK (1999) Electrophysiological evidence for the role of substance P in retinohypothalamic transmission in the rat. Neurosci Lett 274:99-102.

[106] Mick G, Maeno H, Kiyama H, Tohyama M (1994) Marginal topography of neurons expressing the substance P receptor in the rat suprachiasmatic nucleus. Brain Res Mol Brain Res 21:157-161.

[107] Otori Y, Tominaga K, Fukuhara C, Yang J, Yamazaki S, Cagampang FR, Okamura H, Inouye ST (1993) Substance P-like immunoreactivity in the suprachiasmatic nucleus of the rat. Brain Res

619:271-277.

[108] Hartwich M, Kalsbeek A, Pévet P, Nürnberger F (1994) Effects of illumination and enucleation on substance-P-immunoreactive structures in subcortical visual centers of golden hamster and Wister rat. Cell Tissue Res 277:351-361.

[109] Ding JM, Chen D, Weber ET, Fairman LE, Rea MA, Gillette MU (1994) Resetting of the biological clock: mediation of nocturnal circadian shifts by glutamate and NO. Science 266:1713-1717.

[110] Hamada T, Yamanouchi S, Watanabe A, Shibata S, Watanabe S (1999) Involvement of glutamate release in substance P-induced phase delays of suprachiasmatic neuron activity rhythm in vitro. Brain Res 836:190-193.

[111] Ding JM, Chen D, Weber ET, Fairman LE, Rea MA, Gillette MU (1994) Resetting of the biological clock: mediation of nocturnal circadian shifts by glutamate and NO. Science 266:1713-1717.

[112] Morin LP, Blanchard J, Moore RY (1992) Intergeniculate leaflet and suprachiasmatic nucleus organization and connections in the golden hamster. Vis Neurosci 8:219-230.

[113] Swann JM, Macchione N (1992) Photoperiodic regulation of substance P immunoreactivity in the mating behavior pathway of the male golden hamster. Brain Res 590:29-38.

[114] Reuss S, Burger K (1994) Substance P-like immunoreactivity in the hypothalamic suprachiasmatic nucleus of Phodopus sungorus--relation to daytime, photoperiod, sex and age. Brain Res 638:189-195.

[115] Jagota A, de la Iglesia HO, Schwartz WJ (2000) Morning and evening circadian oscillations in the suprachiasmatic nucleus in vitro. Nat Neurosci 3:372-376.

[116] Shibata S, Moore RY (1993) Neuropeptide Y and optic chiasm stimulation affect suprachiasmatic nucleus circadian function in vitro. Brain Res 615:95-100.

Appendix

Ⅰ.List of Journal Publications

A. Published

1) Title: Complex Periodic Spirals and Line-Defect Turbulence in a Chemical System

Authors: Jin-Sung Park and Kyoung J. Lee

Name of Journal (Publication Date): **Physical Review Letters 83**, 5393 (Dec. 1999)

Impact Factor of the Journal and Number of Citation: 6.462 (3)

2) Title: Superlattice, Rhombus, Square, and Hexagonal Standing Waves in Magnetically Driven Ferrofluid Surface

Name of Journal (Publication Date): **Physical Review Letters 84**, 5316 (June 2000)

Impact Factor of the Journal and Number of Citation: 6.462 (2)

Authors: Hyun-Jae Pi, So-yeon Park, Jysoo Lee, and Kyoung J. Lee

3) Title: Substance P Plays a Critical Role in Photic Resetting of the Circadian Pacemakers in the Rat Hypothalamus

Name of Journal (Publication Date): **Journal of Neuroscience 21**, 4026 (June 2001)

Impact Factor of the Journal and Number of Citation: 8.502 (0)

Authors: D. Y. Kim, H.-C Kang, H. C. Shin, Kyoung J. Lee, Y. W. Yoon, H. C. Han, H. S. Na, S. K. Hong, Y. I. Kim

4) Title: Resetting wave forms in Dictyostelium territories

Name of Journal (Publication Date): **Physical Review Letters** (to appear on July 30, 2001)

Impact Factor of the Journal and Number of Citation: 6.462 (0)

Authors: Kyoung J. Lee, R. E. Goldstein, and E. C. Cox

5) Title: Does Hard Core Interaction Change Absorbing-Type Critical Phenomena?

Name of Journal (Publication Date): **Physical Review Letters 85**, 1682 (August 2000)

Impact Factor of the Journal and Number of Citation: 6.462 (7)

Authors: S. Kwon, Jysoo Lee, and H. Park

6) Title: Complex dynamics of a spiral tip in the presence of an extrinsic local modulation

Name of Journal (Publication Date): **Physical Review E 62**, 4799 (October 2000).

Impact Factor of the Journal and Number of Citation: 2.142 (0)

Authors: Seong-min Hwang, Won Gyu Choe, and Kyoung J. Kee

7) Title: Nonlinear correction to Darcy's law for a flow through periodic arrays of elliptic cylinders

Name of Journal (Publication Date): **Physica A 293**, 13 (2001)

Impact Factor of the Journal and Number of Citation: 1.205 (0)

Authors: J. Kim, Jysoo Lee, and K. -C. Lee

8) Title: Network model for deep bed filtration

Name of Journal (Publication Date): **Physics of Fluids 13,** 1076 (May, 2001)

Impact Factor of the Journal and Number of Citation: 1.442 (0)

Authors: Jysoo Lee and J. Koplik

B. Accepted

C. In Press

D. Submitted

1) J. Park and Kyoung J. Lee, "Formation of spiraling line-defects and its meandering transition in a period-2 medium," submitted to Phys. Rev. Lett.

2) H. Ko, Jysoo Lee, and Kyoung J. Lee, "Successive spatial period-doublings in magnetically driven ferrofluid surface," submitted to Phys. Rev. Lett.

3) J. Jeong et. al, "The effect of photic and auditory stimulation on nonlinear dynamics of the human electroencephalogram," submitted to Neuroscience Letters.

4) J. Jeong et. al, "The effect of anesthesia on nonlinear dynamics of DA neurons," submitted to Neuroscience Letters.

5) J. Jeong et. al, "Burst as a source of nonlinear determinism in interspike interval firing patterns of Nigral Dopamine neurons," submitted to Phys. Rev. Lett.

6) J. -H. Kim et. al, "Quasi-periodic motion of spirals in a parametrically modulated liquid crystal layer," submitted to Europhys. Lett..

7) J. Kim et. al, "Harmonic forcing of an extended oscillatory system: homogeneous and periodic solutions," submitted to Phys. Rev. E.

Ⅱ.List of Conference Publications

A. Invited Talks

1) Gordon Research Conference on Nonlinear Science, MA, USA, June 2001.

2) Recent Clinical and Research Advances in Arrhythmias, Seoul, May 2001.

3) KIAS-APCTP Winter Workshop on Biocomplexity, Seoul, Feb. 2001.

4) Int'l Chemical Congress of Pacific Basin Societies Conference (PACIFICHEM2000: Nonlinear Dynamics in Chemistry), Hawaii, USA, Dec. 2000.

5) American Physical Society March Meeting (Sec. B25: Pattern Formation and Dynamics), Minneapolis, USA, March 2000.

6) APCTP Intl. Workshop on Stochastic Dynamics & Pattern Formation in Biological Systems, Seoul, July 1999.

7) Univ. of California at Berkeley, USA, seminar (host: Prof. E. Knobloch), Aug. 1999.

8) Caltech, USA, seminar (host: Prof. J. Pine), Aug. 1999.

9) Kyoto University, Japan, seminar (host: Prof. Y. Kuramoto), Jan. 1999.

10)NTT, Japan, seminar (host: Dr. A. Kawana), Jan. 1999.

B. Contributed Papers(Oral/Poster)

Ⅲ.Patents & Program registered

A. Registered

B. In progress

Ⅳ.Researchers

A. Professors

1) Lee, Kyoung-Jin (Dept. of Physics, Korea Univ., Professor)

B. Research Professors

1) Lee, Jysoo (PhD., 1998.10 ~ 2001.9, KISTI)

2) Choe, Won-Gyu (PhD., 1998.10 ~ 2000.9, Nagoya Univ.)

3) Hwang, Jong-Moon (PhD., 1998.10 ~ 1999.9, Korea Univ.)

4) Kim, Jong-Nam (PhD, 1999.10 ~ 2000.8, Seoul Nat'l Univ.)

5) Shin, Jong-Chul (PhD., 2000.10 ~ 2001.10)

6) Jeong, Jaeseung (PhD, 2001.2 ~)

C. Collaborating Professors

1) Kim, Yang-In (Medical School, Korea Univ., Professor)

2) Pak, Jung-Ho (Dept. of Elec. Eng., Korea Univ., Professor)

3) Ahn, Dong-Jun (Dept. of Chem. Eng., Korea Univ., Professor)

Ⅴ.Others